

# **Diffuse Galactic Light in a high Galactic latitude cloud**

Nobuyuki Ienaka

Department of Astronomy, Graduate School of Science,  
The University of Tokyo

February, 2013



# Abstract

Diffuse Galactic Light (DGL) is the starlight scattered off by dust grains in the Galactic interstellar medium. The DGL is observed in optical wavelengths as a counterpart of the “infrared cirrus” that is diffuse far-infrared thermal emission from interstellar dust. Observations of the DGL along with that of the thermal emission from the same dust cloud would give us an important information about dust properties and interstellar radiation field (ISRF) incident on the dust grains.

Recent observations suggest that the optical and  $100\mu\text{m}$  surface brightness are linearly correlated. However, only a few observations reported such correlations clearly. Especially, a correlation within an individual cloud has not been reported since 1990’s. The major cause of difficulties on observations of the DGL is separation of the foreground emission, which is much brighter than the DGL.

In this thesis, we present our observation of the DGL in a high Galactic latitude cloud. Our goal is to acquire the most accurate measurements ever by utilizing a modern wide-field CCD equipment, and to evaluate uncertainty that arise from foreground separation.

We have conducted  $B$ ,  $g$ ,  $V$ , and  $R$ -band imaging in a  $45' \times 40'$  field containing part of high Galactic latitude translucent cloud MBM32 and careful analysis has performed to extract the diffuse component only. We found excellent, near-linear correlations between the diffuse optical light and the  $100\mu\text{m}$  brightness. A minimum  $\chi^2$  analysis is applied to fit a linear function to the measured correlation and derive the slope parameter  $b(\lambda) = \Delta S_\nu(\lambda)/\Delta S_\nu(100\mu\text{m})$  of  $(1.6 \pm 0.1) \times 10^3$ ,  $(2.2 \pm 0.1) \times 10^3$ ,  $(4.0 \pm 0.3) \times 10^3$ , and  $(3.4 \pm 0.2) \times 10^3$  at  $B$ ,  $g$ ,  $V$ , and  $R$ -band, respectively. This results are the first example which shows the spectra of  $b(\lambda)$  value for an individual cloud. In the course of analysis, we developed a method to evaluate and correct the errors of the flat-fielding for diffuse objects.

We discussed our results in the context of a variety of similar results or theoretical models taken from the literature. We found that the  $b(\lambda)$  values in literature vary by factor of 2, and this variation can be explained by the variations of optical depth along with the sightlines. We also found that our  $b(\lambda)$  spectrum favors the ERE in the diffuse optical light;  $b(\lambda)$  rises from B to V faster than the models, seems to peak around 6000 Å and decreases towards long wavelengths. Such characteristic is expected from the models in which the scattered DGL combined with the ERE.

# Contents

<b>Abstract</b>	<b>iii</b>
<b>1 Introduction</b>	<b>1</b>
1.1 Diffuse sky brightness . . . . .	1
1.1.1 Airglow . . . . .	3
1.1.2 Zodiacal light . . . . .	4
1.1.3 Faint stars . . . . .	7
1.1.4 Diffuse Galactic Light . . . . .	7
1.1.5 Extragalactic Background Light . . . . .	10
1.2 Historical review of DGL observations . . . . .	12
1.2.1 Recent observation . . . . .	13
1.3 Purpose and organization of the thesis . . . . .	20
<b>2 Observations and Reduction</b>	<b>21</b>
2.1 Observation . . . . .	21
2.2 Data processing . . . . .	22
2.2.1 Flat-fielding . . . . .	23
2.2.2 Flux-scaling . . . . .	24
2.2.3 Masking of stars and galaxies . . . . .	25
2.2.4 Aperture correction . . . . .	25
2.2.5 Reducing the resolution . . . . .	30
2.2.6 Zodiacal light subtraction . . . . .	30
<b>3 Analysis and Results</b>	<b>34</b>
<b>4 Discussion</b>	<b>37</b>
4.1 Variations in slope parameter $b(\lambda)$ . . . . .	38
4.1.1 Optical depth and dust albedo . . . . .	38
4.1.2 Dust Temperature . . . . .	42
4.1.3 Latitude and longitude . . . . .	43
4.2 Scattering Models . . . . .	45
4.2.1 Extended red emission . . . . .	45
4.2.2 DGL in the near infrared . . . . .	47
<b>5 Summary</b>	<b>48</b>

<b>Appendix A Flat-fielding</b>	<b>51</b>
A.1 Observations . . . . .	52
A.2 Method . . . . .	55
A.3 Results . . . . .	56
A.4 Summary . . . . .	57
<b>Appendix B Radiative transfer in a dusty slab</b>	<b>62</b>
<b>Acknowledgements</b>	<b>64</b>
<b>Bibliography</b>	<b>65</b>

# Chapter 1

## Introduction

The light from the night sky consists of many components such as, direct starlight, scattered starlight, atmospheric airglow. Regarding observations of point or discrete sources, all diffuse components are subtracted and ignored as a background sky brightness. However, in modern astronomy, diffuse components of the night sky became an important subject. For example, scattered starlight by interplanetary and interstellar dust grains give us an important information about dust properties and radiation field incident on the dust grains. Another important subject is extragalactic background light (EBL) which represents a total brightness of the light comes from outside the Galaxy. The EBL records total energy released by stellar nucleosynthesis or, if any, non-stellar processes over cosmic history. Thus it gives us crucial information about star-formation history in the universe.

Among many diffuse components, this thesis focus on the Diffuse Galactic Light (DGL) which is a scattered starlight by dust grains in interstellar medium. The study of the DGL lead to develop understanding the dust properties and interstellar radiation field. Moreover the DGL is very important to the observation of the EBL, since it contributes to the foreground emission and has to be removed precisely.

### 1.1 Diffuse sky brightness

Figure 1.1 (Leinert et al. 1998) shows an overview on the brightness of the sky from 0.1 to 10000  $\mu\text{m}$ . In the range of optical wavelengths, there are five diffuse components as follows:

- Terrestrial airglow (indicated with  $\text{O}_2$  and  $\text{OH}$  in Figure 1.1)
- Zodiacal light
- Faint stars

- Diffuse galactic light (indicated with "Cirrus" in Figure 1.1)
- Extragalactic background light (not printed in Figure 1.1).

These are listed in descending order of distance from its emitting origin, and that is roughly correspond to the order of brightness. All these components have to be distinguished and separated in DGL observations. Their properties are summarized below.

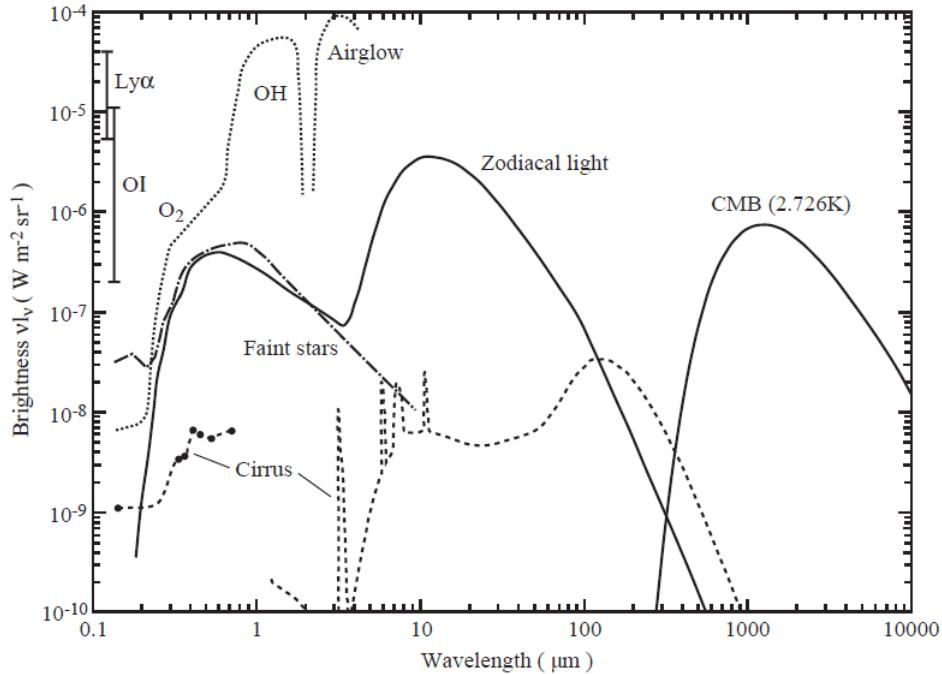


Figure 1.1 Overview on the brightness of the sky outside the lower terrestrial atmosphere and at high ecliptic and galactic latitudes (Leinert et al. 1998). The zodiacal emission and scattering as well as the integrated light of stars are given for the South Ecliptic Pole ( $l = 276^\circ, b = -30^\circ$ ). The bright magnitude cut-off for the stellar component is  $V = 6.0$  mag for  $0.3 - 1 \mu\text{m}$ . In the infrared, stars brighter than 15 Jy between 1.25 and  $4.85 \mu\text{m}$  and brighter than 85 Jy at  $12 \mu\text{m}$  are excluded. No cut-off was applied to the UV data,  $\lambda \leq 0.3 \mu\text{m}$ . The interstellar cirrus component is normalized for a column density of  $10^{20}$  H-atoms  $\text{cm}^2$  corresponding to a visual extinction of 0.053 mag. This is close to the values at the darkest patches in the sky. Source for the long-wavelength data,  $\lambda \geq 1.25 \mu\text{m}$ , are COBE DIRBE and FIRAS measurements as presented by Désert et al. (1996). The IR cirrus spectrum is according to the model of Désert et al. (1990) fitted to IRAS photometry. The short-wavelength data,  $\lambda \leq 1.0 \mu\text{m}$ , are from the following sources: zodiacal light: Leinert & Grun (1990); integrated starlight:  $\lambda \leq 0.3 \mu\text{m}$ , Gondhalekar (1990),  $\lambda \geq 0.3 \mu\text{m}$ , Mattila (1980); cirrus:  $\lambda = 0.15 \mu\text{m}$ , Haikala et al. (1995),  $\lambda = 0.35 - 0.75 \mu\text{m}$ , Mattila & Schnur (1990), Mattila (1979). The geocoronal Lyman  $\alpha$  (121.6 nm) and the OI (130.4, 135.6 nm) line intensities were as measured with the Faint Object Camera of the Hubble Space Telescope at a height of 610 km (Caulet et al. 1994).

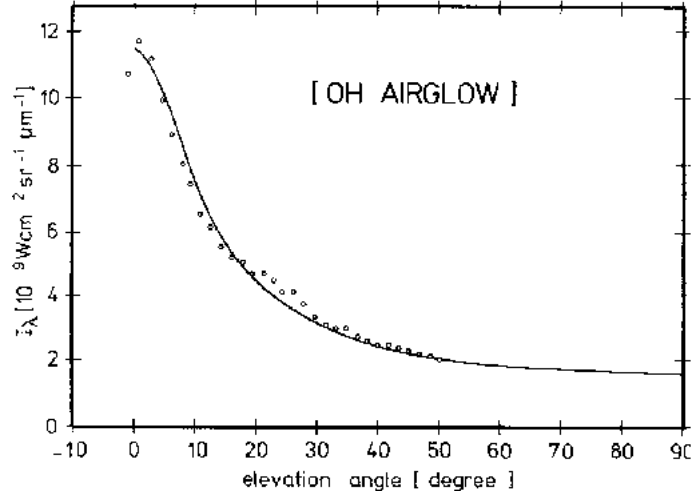


Figure 1.2 Increase of airglow brightness at  $2.1\mu\text{m}$  towards the horizon observed from a balloon at 30 km altitude (Hofmann et al. 1977). Dots represent the measurements, the line gives the van Rhijn function for a height of the emitting layer (E layer) of 92 km.

### 1.1.1 Airglow

The airglow emission comes from the terrestrial atmosphere and constitutes the brightest component of the diffuse light in optical wavelength. The airglow emission varies considerably with time, on short (minutes) and long time-scales, mainly due to changes in the atmosphere and in solar activity, and is the only component which can vary in a single exposure time. The airglow spectrum consists of a number of lines and band emission superposed on a weak continuum. Chamberlain (1961) summarize the main features of the airglow spectrum and Broadfoot & Kendall (1968) give the observed spectrum in optical wavelength (310 nm-1.0  $\mu\text{m}$ ) based on photoelectric observations at Kitt Peak near the zenith and within  $30^\circ$  of the galactic pole. Their observations show that the brightness of the airglow increases with wavelength and emissions from molecular oxygen are dominant in blue band ( $\leq 500$  nm), emissions from atomic oxygen and OH molecule are dominant in green and red band ( $\geq 500$  nm). Most of these emissions arise in the relatively thin layer at an altitude of  $\sim 90$  km, which is known as the ionospheric E layer. Assuming a thin homogeneously emitting layer, latitude dependence of the airglow can be given the so-called *van Rhijn function*

$$I(z)/I(\text{zenith}) = \frac{1}{\sqrt{1 - [R/(R+h)]^2 \sin^2 z}} \quad (1.1)$$

where  $z$  is the angle measured from the zenith,  $R$  is the radius of the earth,  $h$  is the height of the emitting layer. Using this function and values of  $R = 6400$  km,  $h = 100$  km, the spatial variation at  $z = 15^\circ$  is 0.5 % per degree. Figure 1.2 shows airglow brightness from a

balloon observation and the van Rhijn function for a height of the emitting layer (E layer) of 92 km, demonstrating that the equation is well fit the observed data. However, this model does not work well for large zenith distances ( $z > 40^\circ$ ), because it does not take the effect of extinction and scattering into account. Moreover, in ground-based observations, spatial variation in brightness due to the atmosphere conditions are generally exceeds the dependence on the zenith distance (Roach & Gordon 1973), and so the spatial variations in brightness within a few degrees area is more or less random.

### 1.1.2 Zodiacal light

The zodiacal light (ZL) is a diffuse component arising from the interplanetary dust grains. The ZL is composed predominately of thermal emission in mid- and far-IR wavelength, and scattered sunlight in optical and near-IR wavelength. In observations from the earth, the ZL is the second brightest diffuse light and it can sometimes be seen with naked eyes on a sufficiently dark night. The most of interplanetary dust is concentrated within the plane of the inner solar system near the sun, therefore, the strength of the ZL depends on the position of observer and the viewing direction respect to the Sun ( $\lambda - \lambda_\odot, \beta$ ; see Figure 1.3). Using the data from the spacecraft Pioneer 10, Hanner et al. (1974) find that the ZL brightness at the heliocentric distance  $R = 2.41$  AU is less than 10% of that observed at  $R = 1$  AU. The viewing direction dependence of the ZL was also examined and the map of zodiacal light brightness at  $R = 1$  AU in optical wavelength was given by Dumont & Sanchez (1976), Levasseur-Regourd & Dumont (1980), and Levasseur-Regourd (1996). The variation of the ZL brightness within the field of view of a few degree is also depends on the viewing direction and not necessarily negligible compared with the DGL. Therefore, in the observation of the DGL, one must consider the effect of the ZL. The spectrum of the ZL is roughly similar to that of the sun (see upper panel of Figure 1.4.) However the strict ZL spectrum is redder than the solar spectrum as shown in lower panels of Figure 1.4. The observed ZL brightness at several wavelengths are also presented in Table 1.1.

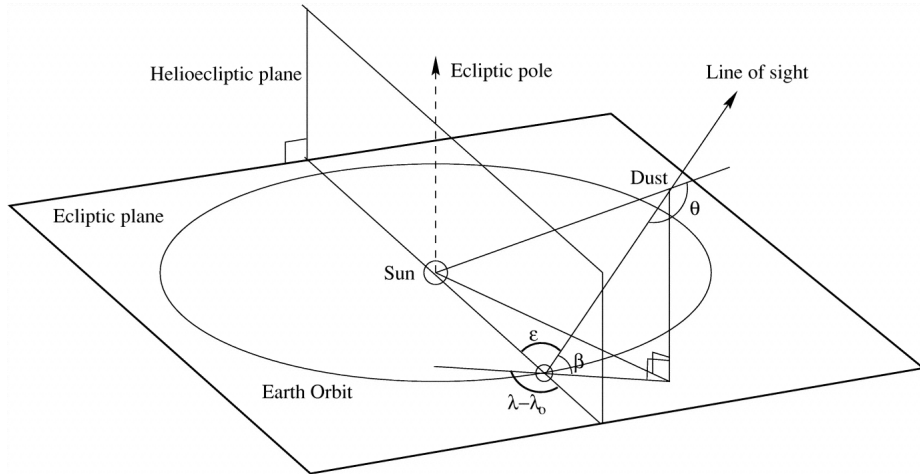


Figure 1.3 Basic geometry for the coordinates used for presenting zodiacal light (Matsuura et al. 1995). The heliocentric ecliptic latitude;  $\beta$  and ecliptic latitude;  $\lambda - \lambda_{\odot}$  of the line of sight is defined in this manner.

Table 1.1 Zodiacal light at  $\epsilon = 90^\circ$  in the ecliptic. (Leinert et al. 1998)

$\lambda$ ( $\mu\text{m}$ )	$I_{ZL}(\lambda)$	
	( $10^{-7} \text{ W m}^{-2} \text{ sr}^{-1} \mu\text{m}^{-1}$ )	( $\text{MJy sr}^{-1}$ )
0.2	0.25	0.00036
0.3	5.3	0.017
0.4	22	0.13
0.5	26	0.23
0.7	20	0.35
0.9	13	0.38
1.0	12	0.43
1.2	8.1	0.42
2.2	1.7	0.28

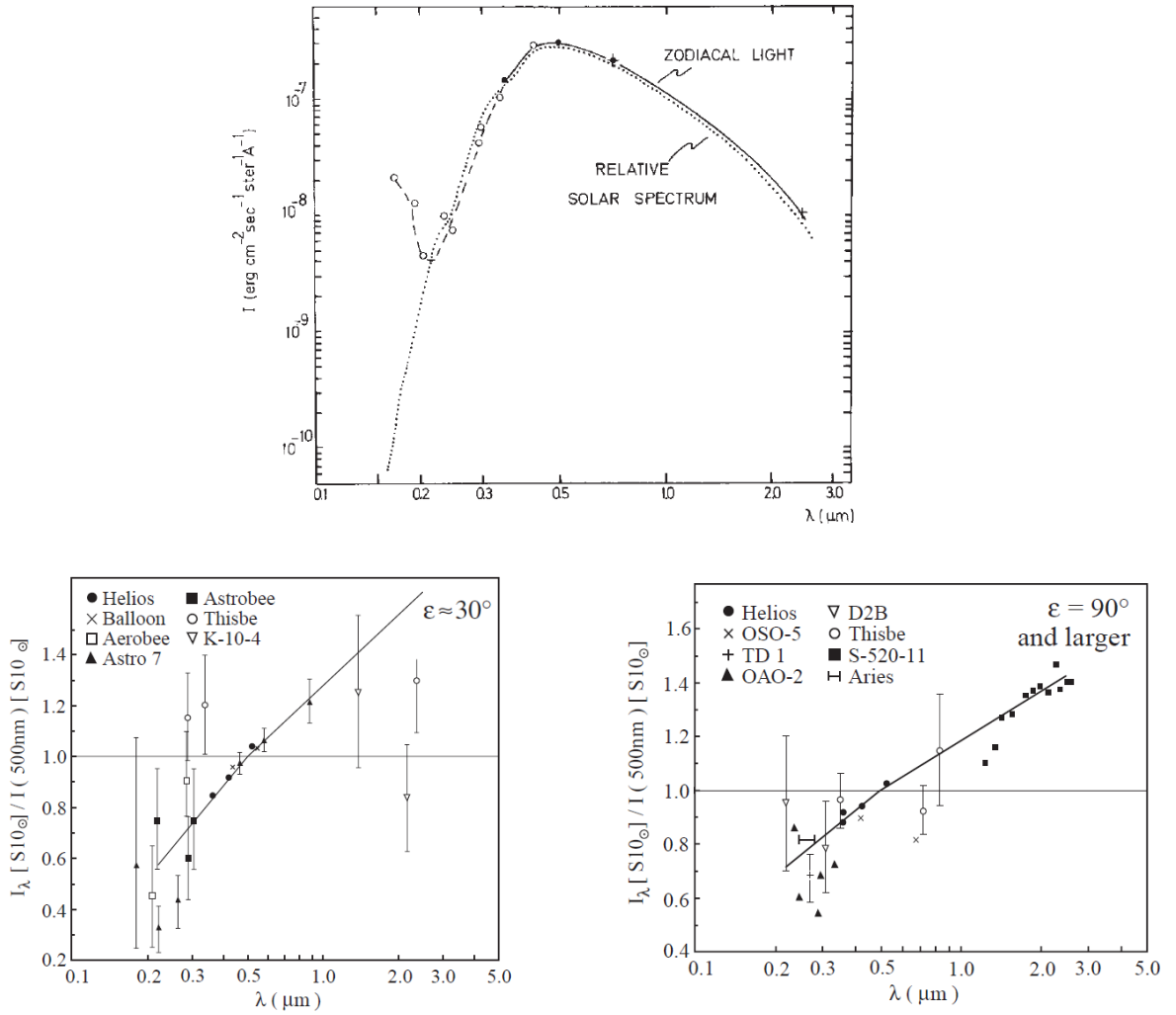


Figure 1.4 The zodiacal light spectrum (Leinert et al. 1998). *Upper panel:* Broadband spectrum of the zodiacal light. Observations by Frey et al. (1974)(filled circle), Hofmann et al. (1973)(plus sign), and Lillie (1972)(open circles) are shown. *Lower panels:* Reddening of the zodiacal light according to color measurements by various space-borne and balloon experiments. The quantity plotted is the ratio of zodiacal light brightness at wave length  $\lambda$  to zodiacal light brightness at wavelength 500 nm, normalized by the same ratio for the Sun. Reddening corresponds to a value of this ratio of  $< 1.0$  for  $\lambda < 500$  nm, and  $> 1.0$  for  $\lambda > 500$  nm. The thick solid line represents the fitted line for the Helios data. The references to the data points are: Leinert & Richter (1981)(Helios), Van de Noord (1970)(Balloon), Feldman (1977)(Aerobee rocket), Pitz et al. (1979)(Astro 7 rocket), Cebula & Feldman (1982)(Astrobee rocket), Frey et al. (1977)(Balloon Thisbe), Nishimura (1973)(rocket K-10-4), Sparrow & Ney (1972a,b)(OSO-5), Morgan et al. (1976)(TD-1), Lillie (1972)(OAO-2),Maucherat-Joubert et al. (1979)(D2B), Matsuura et al. (1995)(rocket S-520-11), Tennyson et al. (1988)(Aries rocket)

### 1.1.3 Faint stars

Besides airglow and the ZL, the integrated light from unresolved stars is the third major contributor of the diffuse night sky brightness in optical wavelength. The integrated starlight contribution to the sky brightness depends on the telescope ability; How faint can the telescope resolve stars, and on the direction of the line of sight; what type of and how many stars are in the line of sight.

In general, the number of stars per unit solid angle decreases with increasing Galactic latitude and therefore the starlight contribution to the diffuse brightness get lower at high Galactic latitude region. Figure 1.5 is a starlight map which constructed by Matsuoka et al. (2011) using two all-sky star catalogs, Tycho-2 Catalog (Høg et al. 2000) and HST Guide Star Catalog II (Lasker et al. 2008), along with a star-count model, TRILEGAL (Girardi et al. 2005). The resolution of this map corresponds to that of the Pioneer 10/11 Imaging Photopolarimeter (IPP). We can see a trend that the brightness decreases towards the Galactic pole on this map. However, the distribution of the starlight is not smooth but have small-scale fluctuations. When we use the instruments with poor resolution, like Pioneer IPP, the total brightness of all stars is observed as a diffuse component. On the other hand, in the observation with the instruments which can resolve stars to some extent, the starlight contribution to the diffuse component is much lower. Figure 1.6 shows fractions of integrated starlight due to stars brighter than a given magnitude, simulated towards the galactic pole with the TRILEGAL code. We can see that almost all flux in the starlight comes from stars brighter than  $\sim 18$  mag in optical wavelength, i.e., the starlight contribution to the diffuse light is very small in the observation with a instrument which can resolve stars fainter than 18th mag. The fluctuation of the diffuse light due to the integrated faint stars is also small, since the numbers of stars which contributes to the diffuse light is large.

### 1.1.4 Diffuse Galactic Light

The Diffuse Galactic Light (DGL) is starlight scattered off by dust grains in the Galactic interstellar medium (ISM). The brightness of the DGL is basically due to the product of the optical depth along the line-of-sight, dust grain's albedo, and the interstellar radiation field (ISRF). In general, the strength of the DGL decreases with increasing Galactic latitude, since the interstellar dust and the intensity of ISRF is concentrated in the Galactic plane. Studies of DGL give useful information about the properties of interstellar dust and the ISFR. Details of the DGL will be described in a later section.

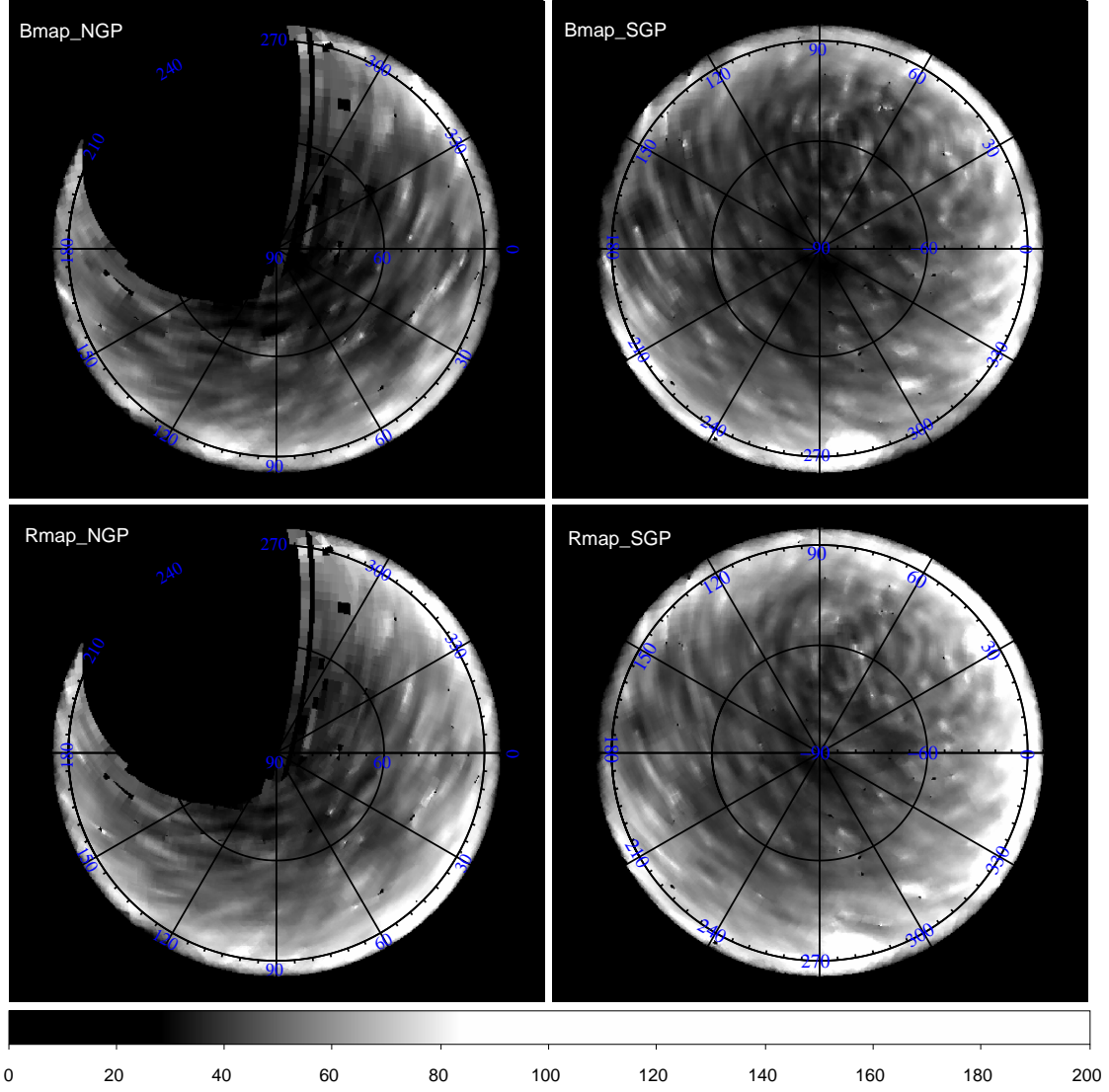


Figure 1.5 Integrated starlight maps (Matsuoka et al. 2011) of the north (*left*) and south (*right*) high Galactic latitude sky ( $|b| > 35^\circ$ ) at  $B_{IPP}$ - (*upper*) and  $R_{IPP}$ -band (*lower*), constructed using two all-sky star catalogs, Tycho-2 Catalog (Høg et al. 2000) and HST Guide Star Catalog II (Lasker et al. 2008), along with a star-count model, TRILEGAL (Girardi et al. 2005). Effective wavelength of the  $B_{IPP}$ - and  $R_{IPP}$ -band are  $0.44$  and  $0.64 \mu\text{m}$ , respectively. The bright magnitude cut-off is  $V = 8$  mag in  $V$ -band. The unit of the brightness is  $\text{MJy sr}^{-1}$ .

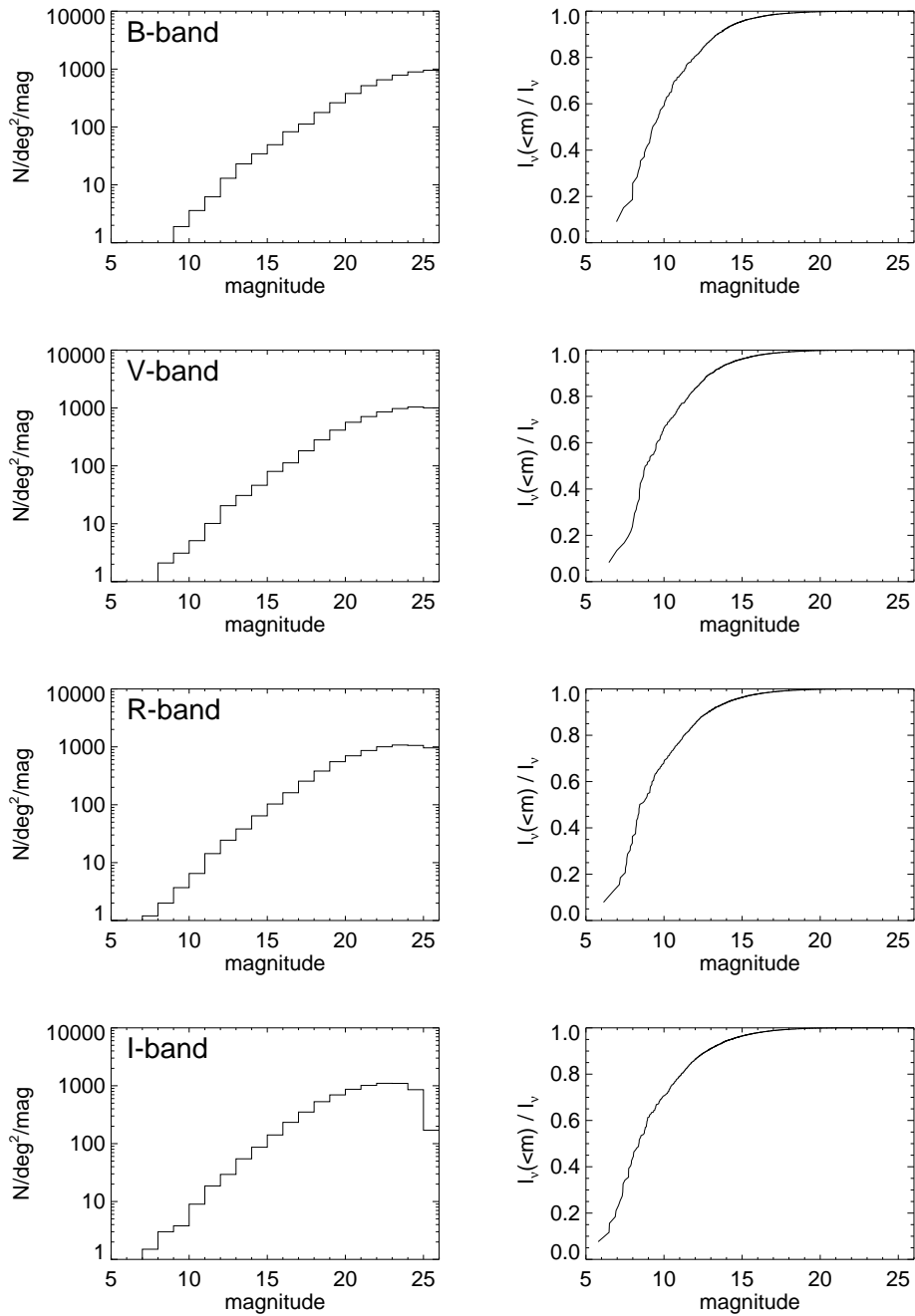


Figure 1.6 Number-counts (*left panels*) and fraction of integrated starlight due to stars brighter than a given magnitude (*right panels*) at galactic pole. Calculation was performed by TRILEGAL (Girardi et al. 2005) adopting the default set of parameters. Each row is for a different broadband,  $B$ ,  $V$ ,  $R$ , and  $I$  from top to bottom.

### 1.1.5 Extragalactic Background Light

The accurate measurement of the DGL along with the other diffuse light described above would lead us to acquire critically important cosmological data, the extragalactic background light (EBL). The EBL at optical wavelength records the total emission from stars in galaxies and any light-emitting materials in the intergalactic space if any, over all time after  $z \sim 6$ . Thus, it has vital information of formation of galaxies, AGNs, and large-scale structure. For example, Fardal et al. (2007) showed that the EBL can be an important test of the global star-formation history. However, the observations of the EBL has been hampered by the strong foregrounds, such as the ZL and the DGL. Figure 1.7 shows the current measurements of the EBL. The filled symbols represents total brightness of the EBL and the open symbols represents the integrated brightness of galaxies, which is a strict lower limit of the EBL. Recently, Bernstein (2007) and Matsuoka et al. (2011) reported the detection of the EBL at optical wavelength. However, their results differ substantially from each other. The results of the former are nearly one order of magnitude larger than the integrated brightness of galaxies and seem to be hard to explain in the current framework of galaxy evolution. On the other hand, the results of the latter are about equal to the integrated brightness of galaxies and consistent with the report that Totani et al. (2001) demonstrate that 60 -90% and 80 - 100% of the total light from galaxies have been resolved at 0.45 and 0.61  $\mu\text{m}$ . In order to reach a firm conclusion on the brightness of the EBL, more extensive studies including the understanding of the DGL as a foreground emission are required.

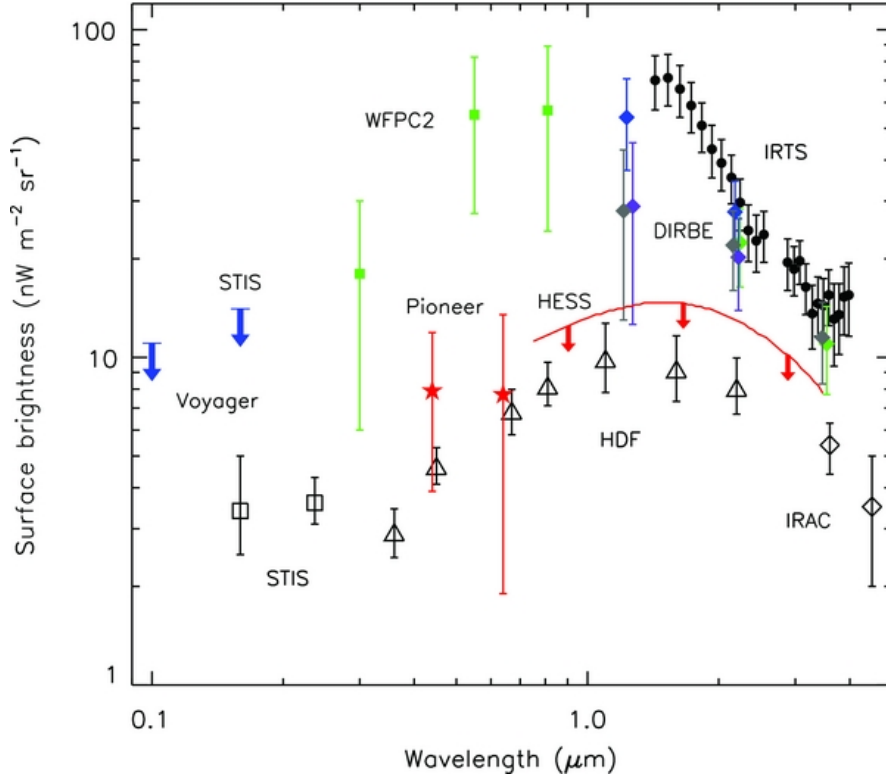


Figure 1.7 Current measurements of the EBL from UV to near-IR (Matsuoka et al. 2011). The filled symbols represents total brightness of the EBL and the open symbols represents the integrated brightness of galaxies. The EBL measurements consist of the UV upper limits (*blue arrows*) at  $0.10 \mu\text{m}$  obtained from the *Voyager/UVS* (Edelstein et al. 2000) and at  $0.16 \mu\text{m}$  from the *HST/STIS* (Brown et al. 2000), the claimed detections at optical wavelengths using the *HST/WFPC2* (Bernstein 2007, *green squares*) and *Pioneer/IPP* (Matsuoka et al. 2011, *red stars*) and at near-IR wavelengths using the *COBE/DIRBE* (Gorjian et al. 2000, *green*); Wright 2001, *purple diamonds*; Cambr sy et al. 2001, *blue diamonds*; Wright 2004, *gray diamonds*; the wavelengths of these measurements are slightly shifted relative to each other for clarity) and the IRTS (Matsumoto et al. 2005, *black circles*). The red solid line with arrows between  $0.8$  and  $4 \mu\text{m}$  represent the HESS upper limits (Aharonian et al. 2006). The integrated brightness of galaxies come from the *HST/STIS* measurements at UV (Gardner et al. 2000, *squares*), the HDF compilation from UV to near-IR (Madau & Pozzetti 2000, *triangles*), and the *SST/IRAC* measurements at near-IR wavelengths (Fazio et al. 2004, *diamonds*).

## 1.2 Historical review of DGL observations

A diffuse optical component to the Galactic ISM, which is called Diffuse Galactic Light (DGL) or sometimes “optical cirrus,” was noticed in late 1930’s. Extensive studies (e.g., Elvey & Roach 1937; Henyey & Greenstein 1941; van de Hulst & de Jong 1969; Mattila 1979) revealed that the DGL is starlight scattered off into a line-of-sight by dust grains in the diffuse ISM which is illuminated by ISRF. The scattering of starlight is characterized by forward-directing phase functions, which is in agreement with the concentration of the DGL brightness towards the Galactic equator (van de Hulst & de Jong 1969).

Over 50 years later, diffuse far-IR emission, so-called “IR cirrus,” was discovered in the *Infrared Astronomical Satellite (IRAS)* mission (Low et al. 1984). It was quickly shown that the IR cirrus is also visible on photographic material (de Vries & Le Poole 1985; Paley et al. 1991), and suggested that 100  $\mu\text{m}$  brightness is remarkably linear to extinction in a range of up to  $\sim 20 \text{ MJy sr}^{-1}$  (de Vries & Le Poole 1985; Laureijs et al. 1987). Finding good agreement between the structures seen on the optical images and the distribution of the CO emission, Stark (1995) pointed out that the optical images can be used to distinguish variations in the dust column density from those in the molecular column density. These studies indicate that the IR cirrus is the far-IR counterpart of the DGL; far-IR emission in IR cirrus is thermal emission which follows the dust absorption of starlight. This also suggests that a combination of optical and far-IR observations would give a powerful tool for investigating the dust properties as well as the ISRF in diffuse ISM (e.g., Beichman 1987 and references therein; Guhathakurta & Tyson 1989).

Since late 1990s, remarkable progress have been made in the optical and far-IR. In the optical, new wide-field CCD cameras make it possible to cover nearly one square degrees or more at a time, providing the uniform sensitivity over a large area and reducing the systematic uncertainty by temporal airglow variations. In the far-IR, Schlegel et al. (1998), hereafter SFD98, published the *IRAS/DIRBE* maps which are reprocessed all-sky maps, by combining *IRAS* and DIRBE (Diffuse Infrared Background Experiment on board the Cosmic Background Explorer satellite) data. The *IRAS/DIRBE* maps have DIRBE quality calibration and *IRAS* resolution as well as removal of artifacts from the *IRAS* scan pattern. Recent studies of diffuse optical light benefit from the progress using a wide-field CCD camera and/or the *IRAS/DIRBE* maps.

Previous studies, in which optical and far-IR observations are combined, are described below.

### 1.2.1 Recent observation

Laureijs et al. (1987) studied the optical surface brightness of high Galactic latitude cloud Lynds 1642 ( $l=210^{\circ}8$ ,  $b=-36^{\circ}7$ ). They used original IRAS survey maps (HCON3; IRAS Explanatory Supplement 1985). The zodiacal light component has been subtracted by fitting a cosecant law of the form  $I_{\nu}(\beta) = A/\sin(|\beta|)+C$ , where  $\beta$  and  $C$  are ecliptic latitude and constant parameter. Optical data were acquired from photoelectric observation with a circular apertures of a  $88''$  diameter. The stars were excluded by locating the apertures avoiding stars in photoelectric observations. They found a good correlation of the optical surface brightness with the  $100 \mu\text{m}$  surface brightness (see Figure 1.8).

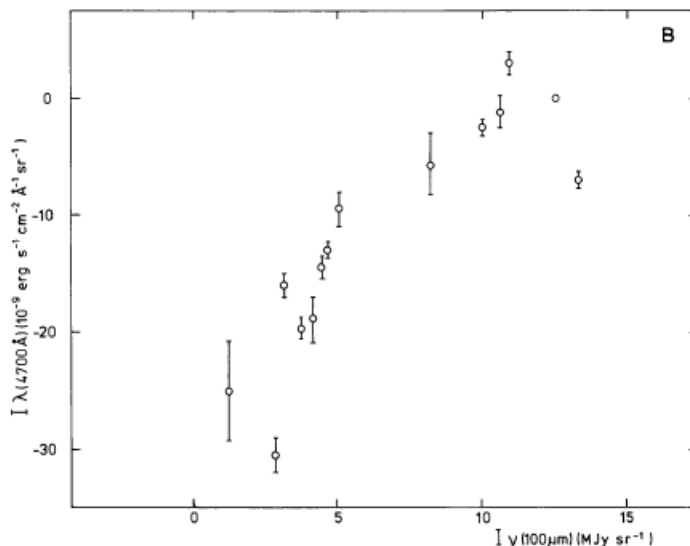


Figure 1.8 Photoelectric surface brightness at  $4700 \text{ \AA}$  versus  $I_{\nu}(100\mu\text{m})$  (Laureijs et al. 1987). The surface brightness at  $4700 \text{ \AA}$  is measured relative to a reference position, which has by definition zero surface brightness.

Guhathakurta & Tyson (1989) observed the edge of four high Galactic latitude clouds ir1 ( $l = 174^{\circ}$ ,  $b = -42^{\circ}$ ), ir2 ( $l = 235^{\circ}$ ,  $b = 37^{\circ}$ ), ir3 ( $l = 38^{\circ}$ ,  $b = 45^{\circ}$ ), and ir4 ( $l = 72^{\circ}$ ,  $b = 25^{\circ}$ ) with three bands ( $B_J$ ,  $R$ , and  $I$ ) using a CCD. The bright stars were clipped out of the image and the faint stars were cleaned by replacing them with the local value of sky. These images were smoothed to an angular resolution of  $3'$ , which is the FWHM of IRAS HCON3 maps, in order to quantitative comparison between the optical and far-IR images. Optical counterparts of the clouds were detected in all four fields. However, their measurements did not show a clear correlation between the optical and far-IR brightness (see Figure 1.9).

Paley et al. (1991) studied a high Galactic latitude compact cirrus ( $l = 38^{\circ}$ ,  $b = -32^{\circ}$ ). The optical data were taken with the CCD/Transit Instrument at three bands ( $B$ ,  $V$ , and

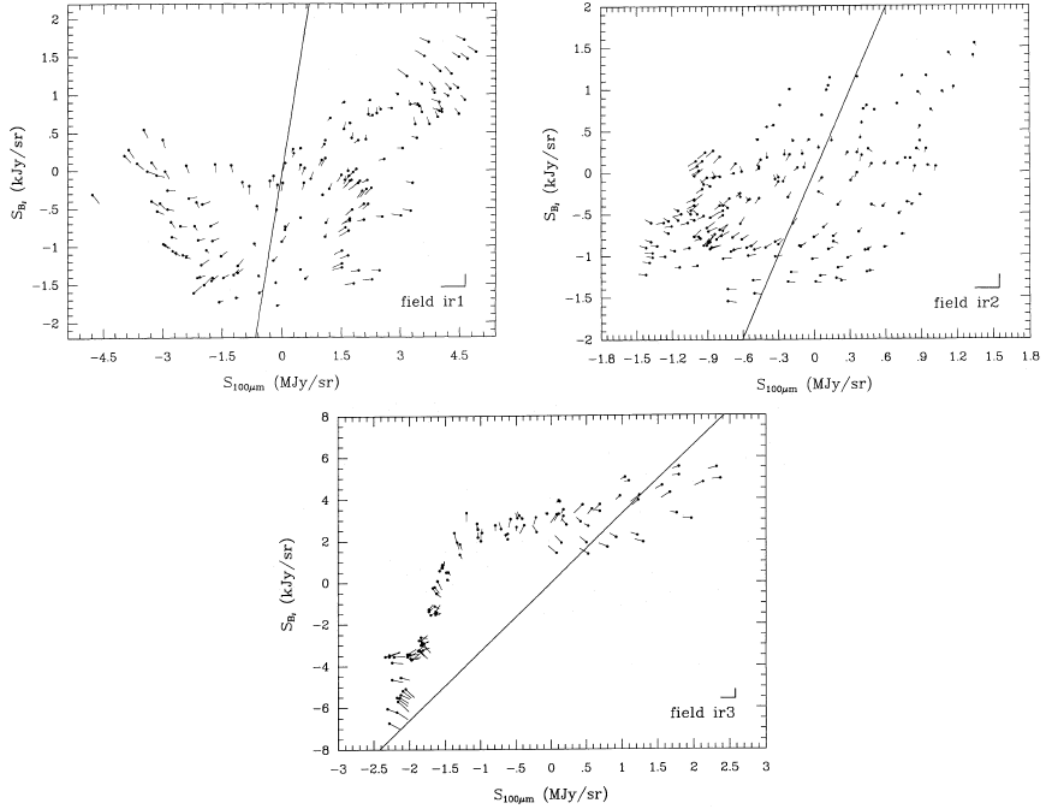


Figure 1.9 Surface brightness at  $B_J$ -band versus  $100 \mu\text{m}$  surface brightness for field ir1 (*top-left*), ir2 (*top-right*), and ir3 (*bottom*) (Guhathakurta & Tyson 1989). An arbitrary background has been subtracted from each of the optical and  $100 \mu\text{m}$  surface brightness. The straight lines has slopes equal to that predicted by a model in which an optically thin dust cloud is isotropically scatters the incident ISRF.

$R$ ). The surface brightness was measured by a rectangular apertures avoiding stars on the median-filtered images. They confirmed the optical counterpart of the infrared cirrus and presented the optical surface brightness correspond to the cirrus cloud by subtracting the local sky brightness.

Zagury et al. (1999) observed a high Galactic latitude cloud MCLD123.5+24.9 ( $l = 123.5^\circ, b = 24.9^\circ$ ) located in the large infrared cirrus known as the Polaris Flare. They observed the cloud with a CCD with  $B$ ,  $V$ , and  $R$  filters. The stars and galaxies on the optical images were subtracted from each image and replaced by an interpolation. Then, in order to compare the optical and  $IRAS$   $100 \mu\text{m}$  map (ISSA plate), the optical images were smoothed to  $IRAS$  resolution. Figure 1.10 is the  $R$ -band image smoothed to  $IRAS$  resolution and Figure 1.11 is the comparison of  $R$ -band and  $100 \mu\text{m}$  emission along the 4 cuts drawn in Figure 1.10. The dotted curves are the  $IRAS$   $100 \mu\text{m}$  brightness and

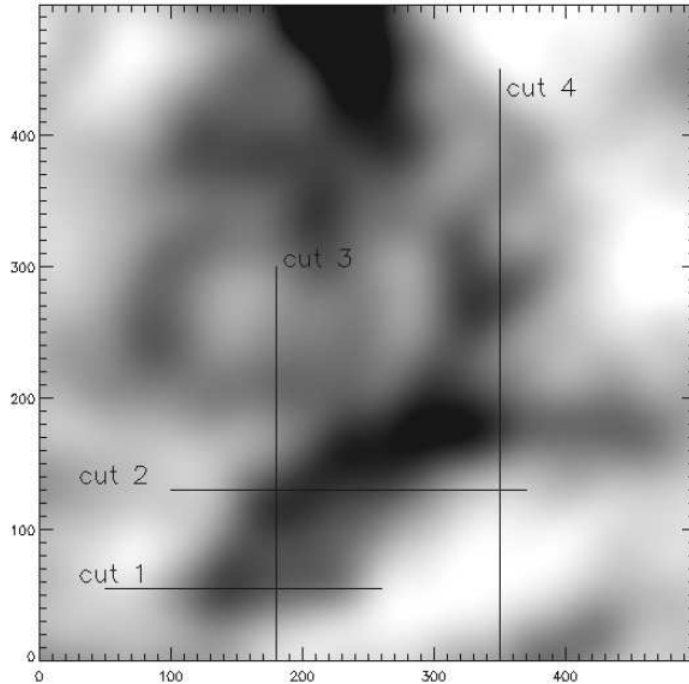


Figure 1.10  $R$ -band image smoothed to  $IRAS$  resolution (Zagury et al. 1999). Numbers on each side of the image refer to pixel numbers.

the dashed lines are the  $R$ -band surface brightness. The  $R$ -band surface brightness was first linearly transformed (divided by  $S_\nu(R)/S_\nu(100\mu\text{m})$  and an appropriate offset) so as to match the  $100\mu\text{m}$  emission. This scaling was done independently within each of the intervals separated by vertical lines indicated in each panel. In each interval, the local value of  $10^3 S_\nu(R)/S_\nu(100\mu\text{m})$  is written on the top of the plot. This figure shows that the structure of the optical brightness is similar to that of the  $100\mu\text{m}$  emission within the scale of a few hundred arcminutes. However, the surface brightness ratios between the optical and the  $100\mu\text{m}$  differs widely within the observed field of view of one square degree. They also showed that the optical brightness, colors, and the surface brightness ratios between the optical and the  $100\mu\text{m}$  can be explained by forward scattering of Polaris light.

Witt et al. (2008) observed five high Galactic latitude clouds MBM25 ( $l = 173.8^\circ, b = 31.5^\circ$ ), MBM30 ( $l = 142.2^\circ, b = 38.2^\circ$ ), MBM32 ( $l = 147.2^\circ, b = 40.7^\circ$ ), 41A ( $l = 90.0^\circ, b = 39.0^\circ$ ), and 41D ( $l = 92.3^\circ, b = 37.5^\circ$ ) at  $B$ ,  $G$ ,  $R$ , and  $I$  with a CCD. They performed photometry by selecting  $18'' \times 18''$  rectangular apertures for cloud and sky avoiding stars as faint as  $\sim 21\text{mag}$ . By comparing to the  $IRAS/DIRBE$   $100\mu\text{m}$  map, they found a linear correlation between the surface brightness in  $B$ -band and that of the  $100\mu\text{m}$  (see Figure 1.12). They also compared the observed optical brightness and the spectral energy distributions

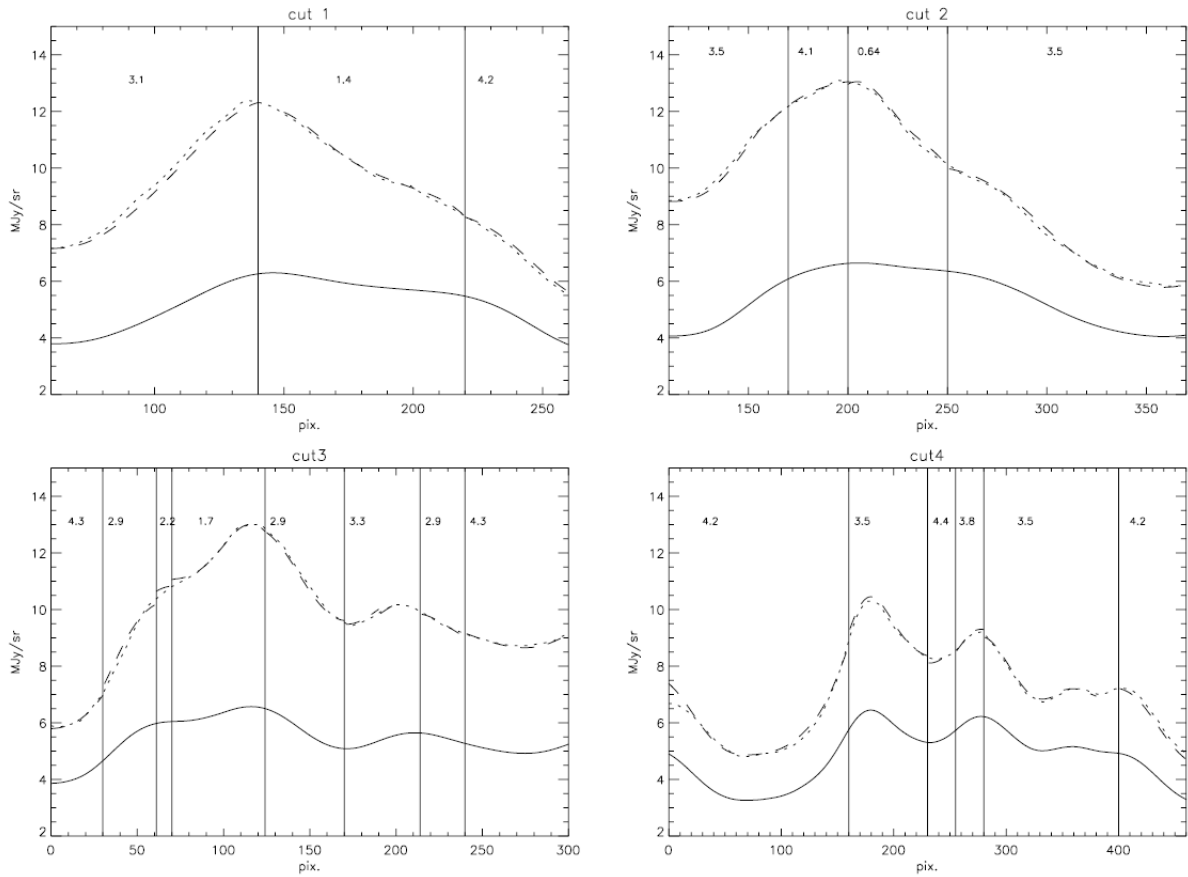


Figure 1.11 Comparison of  $R$ -band and the  $100 \mu\text{m}$  emission along the 4 cuts drawn in upper panel. The dotted curves are the IRAS  $100 \mu\text{m}$  brightness and the dashed lines are the  $R$ -band surface brightness. The  $R$ -band surface brightness was first linearly transformed (divided by  $S_\nu(R)/S_\nu(100\mu\text{m})$  and an appropriate offset) so as to match the  $100 \mu\text{m}$  emission. This scaling was done independently within each of the intervals separated by vertical lines indicated in each lower panel. In each interval, the local value of  $10^3 S_\nu(R)/S_\nu(100\mu\text{m})$  is written on the top of the plot. The solid line at the bottom of each panel is the  $R$ -band brightness multiplied by 155, with an arbitrary offset.

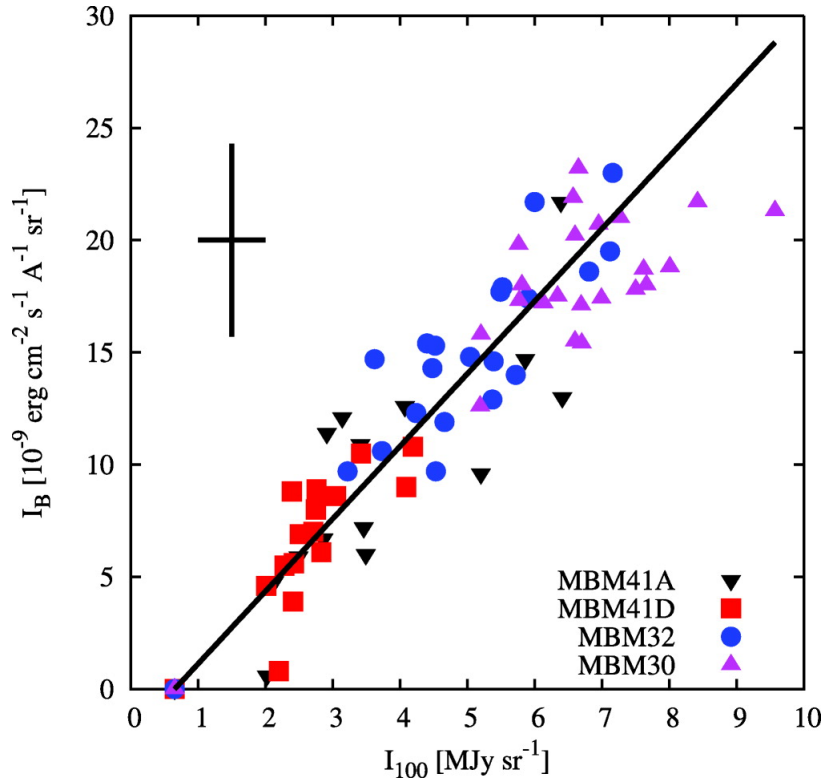


Figure 1.12 Sky subtracted surface brightness at  $B$ -band versus  $100\mu\text{m}$  surface brightness (Witt et al. 2008). The IRAS  $100\mu\text{m}$  brightness at the sky reference level was  $0.65 \text{ MJy sr}^{-1}$ .

expected by scattered light model, and found excess of the observed brightness in  $R$ -band and  $G$ -band. They concluded that these excess brightness and their spectral energy distributions are consistent with the presence of extended red emission (ERE) which represents optical emission from the interstellar dust grains. Details of the ERE is described in section 4.2.1 .

Using the *Pioneer 10/11* Imaging Photopolarimeter data taken beyond the zodiacal dust cloud at  $B$  and  $R$ -band, Matsuoka et al. (2011) found a linear correlation between the optical surface brightness and the *IRAS*/*DIRBE*  $100\mu\text{m}$  surface brightness in regions with low  $100\mu\text{m}$  surface brightness  $< 3.0 \text{ MJy sr}^{-1}$  and at Galactic latitude  $|b| > 35^\circ$ , which corresponds to about a quarter of the whole sky (see Figure 1.13). They derived mean ratios between the optical and the  $100\mu\text{m}$  for a wide area of a quarter of the whole sky for the first time, but not individual clouds.

Brandt & Draine (2012) measured the optical spectrum of the DGL using nearly 90,000 blank-sky spectra from the SDSS, by correlating the optical intensity in regions of blank sky against  $100\mu\text{m}$  intensity. The observed correlation over the interval from  $0.69\mu\text{m}$  to  $0.7\mu\text{m}$  is presented in Figure 1.14. The sky coverage of their data was dominated by Northern

Galactic Cap because SDSS spectroscopy was mainly performed on the regions where the levels of extinction is low. However, the bulk of their measured signal was obtained from the data taken at modest Galactic latitude ( $b = 30 - 45^\circ$ ), where the dust is denser than the high Galactic latitude region and therefore the DGL is stronger. They also calculated

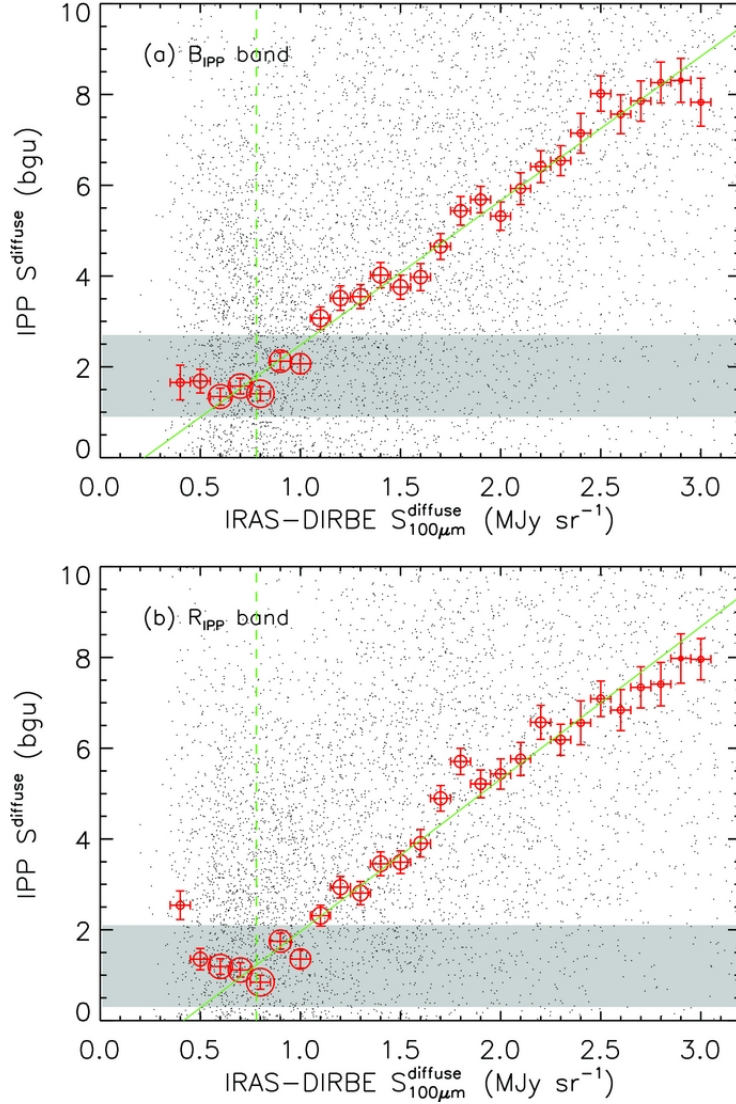


Figure 1.13 Diffuse optical brightness  $S^{diffuse}$  versus the  $100\mu\text{m}$  brightness  $S_{100\mu\text{m}}^{diffuse}$  (dots) seen beyond the zodiacal dust zone by *Pioneer*10/11 (Matsuoka et al. 2011). Upper panel is for  $B_{IPP}$ -band and lower panel for  $R_{IPP}$ -band. The red circles and error bars represent mean values of  $S^{diffuse}$  and their errors in the  $S_{100\mu\text{m}}^{diffuse}$  bins. The sizes of the circles are proportional to the numbers of the data points in the bins. The solid green lines show the regression lines at  $S_{100\mu\text{m}}^{diffuse} > 1.0 \text{ MJy sr}^{-1}$ , while the dashed green lines show the cosmic infrared background (CIB) brightness  $S_{100\mu\text{m}}^{CIB}$  reported by Lagache & Puget (2000). The shaded areas show the  $1\sigma$  confidence intervals of estimates of the EBL brightness.

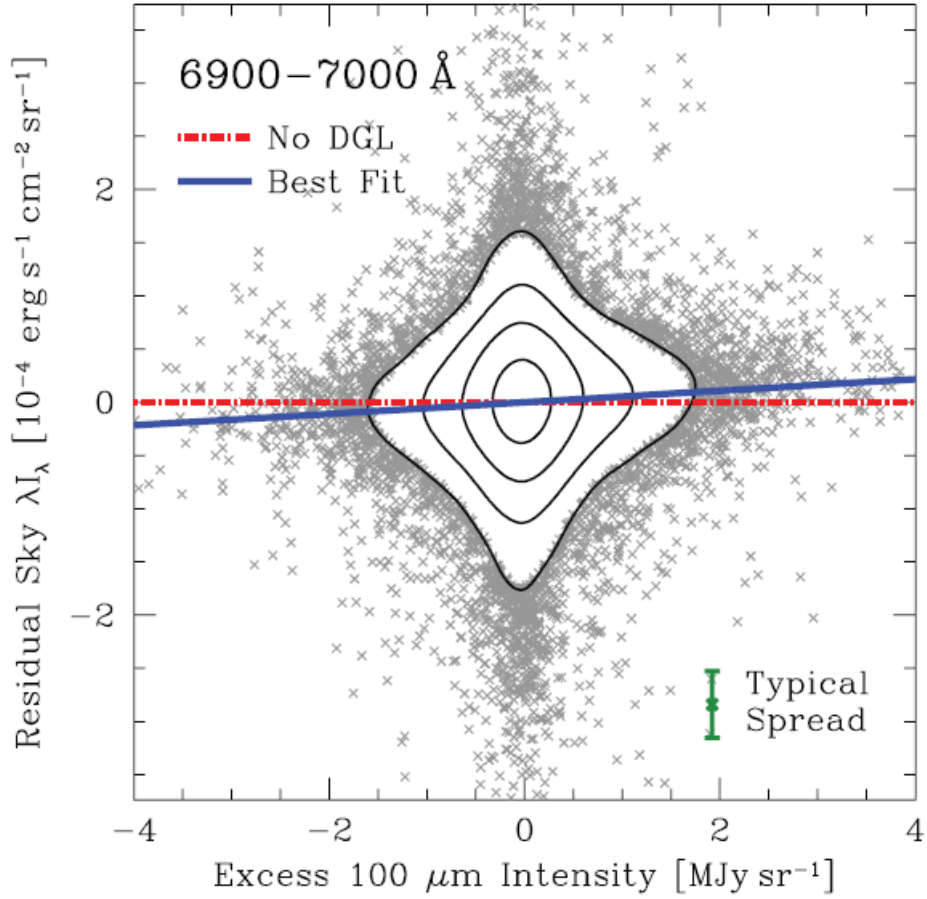


Figure 1.14 The correlation between  $100\mu\text{m}$  intensity relative to the mean over an SDSS sky fiber’s plate and the residual sky intensity averaged over the interval from  $0.69\mu\text{m}$  to  $0.7\mu\text{m}$  (Brandt & Draine 2012). Logarithmically spaced contours were used where the density of points is high. The data demand a non-zero slope, a component of the sky background associated with interstellar dust, at more than  $70\sigma$ .

the model spectra of the DGL adopting a several ISRF and two dust models.

### 1.3 Purpose and organization of the thesis

As described in the previous section, recent observations suggest that the optical and  $100\mu\text{m}$  surface brightness are linearly correlated. However, a clear correlation was only reported by Laureijs et al. (1987), Witt et al. (2008), Matsuoka et al. (2011), and Brandt & Draine (2012). Among these, Laureijs et al. (1987) is the only example of a correlation within a single cloud. As shown in Figure 1.8, the measurements of Laureijs et al. (1987) shows a relatively clear correlation, but these data points were acquired by combining observations with a single channel photoelectric device and simultaneous monitoring observations with photographic plates and their measurement accuracy is not sufficient.

The major cause of difficulties on observations of the DGL is separation of the foreground emission. This may be a reason for no correlations were found in observations other than those listed above. Basically the foreground emission is much stronger than the DGL and its inaccurate removal lead to a large uncertainty. For example: (1) Airglow can be considered as a constant across the field of view. However, if the flat-fielding was inaccurate, the airglow emission would have a significant effect on results (details are described in Section 2.2.1). In previous studies, this effect is not carefully considered; (2) Zodiacal light is also not well considered in previous observations; (3) In most observations, including all four papers that reported clear correlations, flux from stars are excluded by selecting a aperture position so that stars would not be included in the aperture. In this method, positions and number of apertures are limited. Moreover, Brandt & Draine (2012) pointed out that the small aperture size compared to the resolution of the far-IR data result in a bias in correlation slope parameters.

In this thesis, we report results of optical surface brightness measurements of the DGL in a high galactic latitude region, which includes portions of the molecular cloud MBM32. Our goal is to acquire the most accurate measurements ever by utilizing a modern wide-field CCD equipment. And also we evaluate uncertainty that arise from foreground separation.

The thesis consists of three thematic components: first, the report on the new observations, the reduction of the data and their initial analysis; second, a discussion of the new results in the context of a variety of similar results taken from the literature; and third, a discussion concerning the possible detection of extended red emission (ERE) through a comparison of the data with model predictions of the colors of the DGL.

## Chapter 2

# Observations and Reduction

### 2.1 Observation

The target field was selected to have following properties: (1) it is optically thin or translucent in the optical and characterized by a sufficient contrast at  $100\mu\text{m}$ ; (2) it is not crowded with stars and do not include bright stars. The first criterion is to see the correlation clearly and the second is to minimize contamination from stars, especially the extended halo of bright stars. Under these criteria, we have selected south part of a high Galactic latitude cloud MBM32 extending  $\sim 1^\circ \times 1^\circ 5$ . This is a diffuse, translucent molecular cloud with extinction of  $A_V = 0.3 - 0.5$  (Magnani & de Vries 1986), and located at a distance of  $\sim 120$  pc (Magnani et al. 1996) at  $l=147^\circ 2$ ,  $b=40^\circ 7$ . The surrounding sky is not a pure blank-sky and thermal far-IR emission from interstellar dust is detected. Based on the *IRAS*/DIRBE  $100\mu\text{m}$  map, Witt et al. (2008) estimated  $A_V = 0.6$  for the cloud and  $A_V = 0.25$  for the surrounding sky. The  $100\mu\text{m}$  intensity in the field ranges from 1.4 to 7.0 MJy  $\text{sr}^{-1}$ .

The optical data were acquired using the 105cm Schmidt telescope with the 2KCCD camera with  $2048 \times 2048$  pixels (Itoh et al. 2001) at Kiso observatory<sup>1</sup> in dark nights in 2011 February, April, and 2012 February. The Sun and the Moon were more than 35 degrees under the horizon when the data were acquired. The field of view of the camera is  $50' \times 50'$  with a pixel scale of  $1''.5 \text{ pixel}^{-1}$ . The average seeing was  $\sim 3''.3$ . The area of high-quality is approximately  $45' \times 40'$ , smaller than the field of view of the camera due to the dithering.

In Figure 2.1, the observed  $45' \times 40'$  field is indicated with a white square which is superimposed on the *IRAS*/DIRBE  $100\mu\text{m}$  map. Images were obtained at four photometric bands,  $B$ ,  $g$ ,  $V$ , and  $R$ . In order to reduce the effects of large-scale non-uniformity of flat-fielding, we observed the field at two different telescope attitudes by flipping the telescope around the ascension axis in such a way that the difference in hour angle is 180 degrees.

---

<sup>1</sup>Kiso observatory is operated by Institute of Astronomy, The University of Tokyo

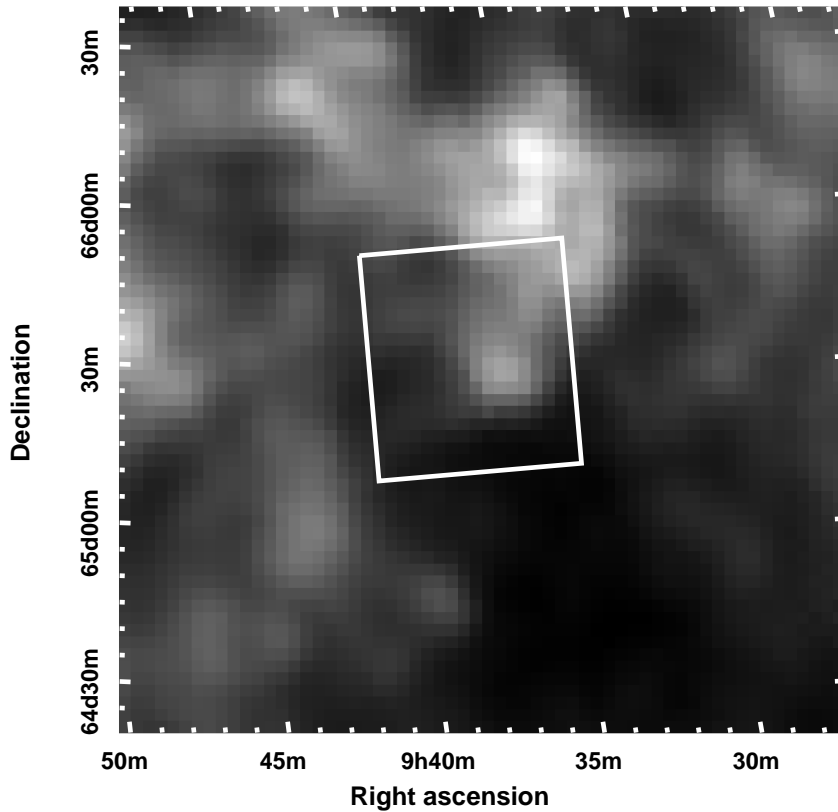


Figure 2.1 Optical field superimposed on the *IRAS*/DIRBE  $100\mu\text{m}$  map. The solid square represents the observed field. The brightest point of the  $100\mu\text{m}$  map is correspond to the center of CO emission of molecular cloud MBM32 (Magnani et al. 1985).

Details of the flat-fielding will be described in following section and appendix. In each telescope attitude, the field was observed three times per photometric band with dithering of a few arcmins. The total exposure time was 1800 sec ( $300 \text{ sec} \times 6$ ) per band.

## 2.2 Data processing

The data reduction was performed in a standard manner, including overscan subtraction, bias subtraction, and flat-fielding with dome-flat, using the IRAF software package <sup>2</sup>.

<sup>2</sup>IRAF is distributed by the National Optical Astronomy Observatory, which is operated by the Association of Universities for Research in Astronomy (AURA) under cooperative agreement with the National Science Foundation.

Table 2.1 Observations and errors.

Band	$\lambda_{center}$ ( $\mu\text{m}$ )	$\sigma(\lambda)^\dagger$ ( $\text{kJy sr}^{-1}$ )	Obs. date (UT)	$ \lambda - \lambda_\odot $ ( $^\circ$ )
<i>B</i>	0.44	0.48	2011-02-04	165
<i>g</i>	0.49	0.39	2011-04-03	107
<i>V</i>	0.55	0.79	2012-02-21	148
<i>R</i>	0.65	0.39	2012-02-21	148
<i>IRAS/DIRBE</i>	100	$0.3 \times 10^3$		

<sup>†</sup>Typical standard deviation for a smoothed  $2'.372 \times 2'.372$  pixel.

### 2.2.1 Flat-fielding

In observations of diffuse components, accurate flat-fielding is very important, because we cannot subtract airglow brightness in such a way that using a reference sky aperture as in the point sources photometry. As an example, let us consider a simple case, a 1-dimensional brightness map including airglow, DGL and a star as indicated in Figure 2.2. The brightness of airglow (*black dashed line*) is about one hundred times larger than that of DGL. The left panel of the Figure 2.2 is the case when the flat-fielding is perfect, the right panel is the case when the flat-fielding has a 5% per degree error. In following analysis in this thesis, the brightness of airglow is assumed to be constant within the observed field. Thus, even if the flat-fielding results in a gradient in the brightness of airglow as shown by *black dashed line* in the right panel, we will estimate the brightness as a constant value as shown by *red dashed line*. Regarding point source photometry, we can subtract the background sky using a nearby area of the star as indicated by *blue lines*. Therefore, the errors of the flat-fielding affect the photometry linearly, i.e, 1% errors of the flat-fielding result in 1% errors of the star flux. In fact, ratio of star flux measured in the left ( $F_{left}$ ) and right ( $F_{right}$ ) panels using the nearby area for sky subtraction is  $F_{right}/F_{left} \sim 1.01$ . However, in diffuse components photometry, incorrect estimation of the airglow brightness make a critical effect, especially in case when the brightness of measuring component is significantly weaker than that of the airglow. The brightness of DGL is shown by shades in the Figure 2.2. Ratio between the brightness of DGL at same position in each panel ( $S_{left}(X)$  and  $S_{right}(X)$ ) is  $S_{right}(100)/S_{left}(100) \sim 0.6$ . The gradients of the DGL measured in each panel are also affected; in left panel  $S_{left}(800)/S_{left}(100) \sim 1.6$ , on the other hand in right panel  $S_{right}(800)/S_{right}(100) \sim 3.1$ .

In order to reduce the effects of large-scale non-uniformity of flat-fielding as much as possible, we evaluate and calibrate the flat images by observing the same sky area by

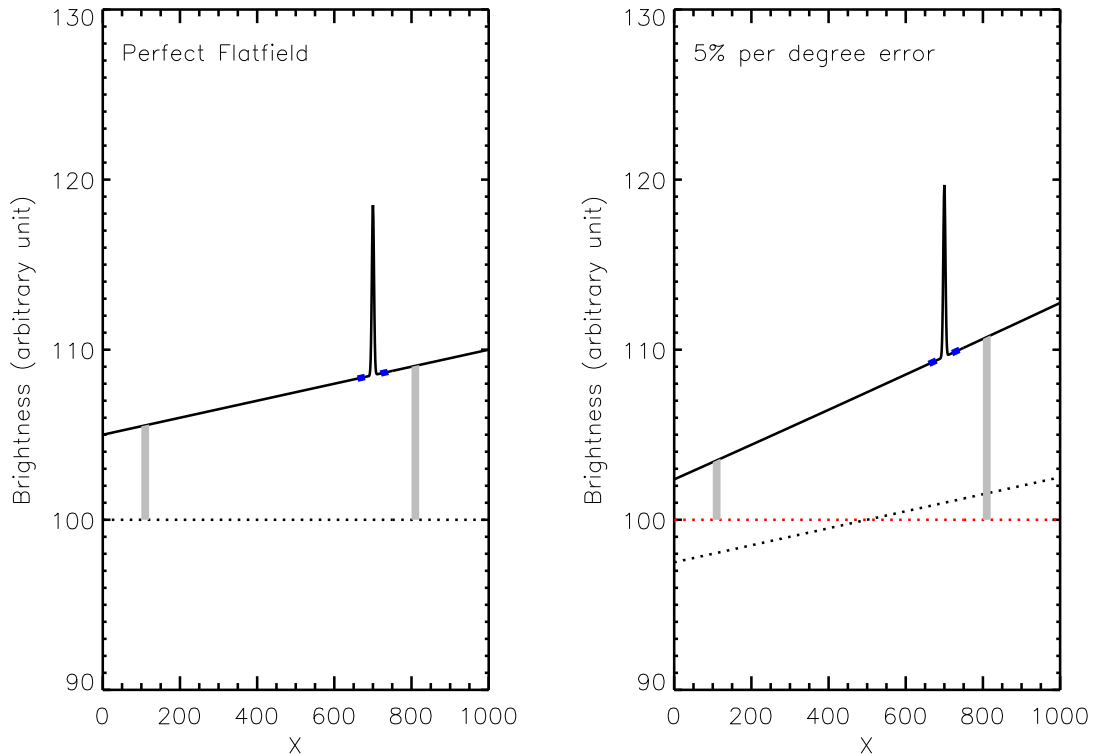


Figure 2.2 1-dimensional brightness map of the model, in which the airglow is constant and the DGL has gradient and a star located at  $X = 700$ , in case of perfect flat-fielding (*left*) and of 5% per degree error (*right*). Brightness of airglow is shown by *black dashed line*. The *red dashed line* represents a misestimated brightness of airglow. Shades are the brightness of the DGL at  $X = 100$  and  $X = 800$ . The *blue lines* are the sky apertures for photometry of the star.

different positions of the CCD and comparing the measured brightness. As a result we found that by observing the target field at two different telescope attitudes; flipping the telescope around the ascension axis by 180 degrees, the error of the flat-fielding could be reduced to  $\sim 0.2\%$ . The details of the evaluation and calibration of the flat images are presented in Appendix.

### 2.2.2 Flux-scaling

The flux-scaling was calibrated by using nearly 1,000 stars in a range of 15-19 mag which are listed in the Sloan Digital Sky Survey (SDSS<sup>3</sup>) Data Release 8 photometric catalogue (Aihara et al. 2011). The SDSS magnitudes (*psfMag*) are transferred to the *BVR*

<sup>3</sup>Funding for SDSS-III has been provided by the Alfred P. Sloan Foundation, the Participating Institutions, the National Science Foundation, and the U.S. Department of Energy Office of Science. The SDSS-III web site is <http://www.sdss3.org/>.

magnitudes (Jester et al. 2005), and then correlated against instrumental magnitudes to derive the zero-points. The SExtractor software package (Bertin & Arnouts 1996) was used with a circular  $8''$  radius aperture. The uncertainty in the zero-points is estimated to be 0.01 - 0.02 mag. The systematic errors introduced through the conversion of magnitudes are approximately 0.03 mag.

### 2.2.3 Masking of stars and galaxies

In order to obtain the diffuse component, we masked stars and galaxies in the images. Masking procedure is as follows. First, we detected all the discrete sources that exceed  $1.5 \sigma$  of the local background in more than 3 continuous pixels using SExtractor with parameters  $DETECT\_THRESH = 1.5$  and  $DETECT\_MINAREA = 3$ . Figure 2.3 shows the histogram of the number of detected sources as a function of magnitude in 1.0 mag bins. Detection limits are below 21 mag in all bands, which is sufficient deepness to remove almost all flux in the starlight (see also Section 1.1.5). The contribution from the stars fainter than 21 mag, calculated using a star-count model TRILEGAL, is  $\sim 0.33 \text{ kJy sr}^{-1}$  at  $B$  and  $\sim 0.39 \text{ kJy sr}^{-1}$  at  $R$ -band. These brightnesses are small compared to that of the DGL ( $\geq 10 \text{ kJy sr}^{-1}$ ). Second, from the detected bright stars, we derived point spread functions (PSFs) by fitting the Moffat function  $I = I_0[1 + (r/\alpha)^{-2}]^{-\beta}$  (Moffat 1969), where  $I_0$  is the intensity at the center of the stellar image and  $\alpha$  and  $\beta$  are the fitting parameters depending on the seeing. Figure 2.4 shows the radial profiles of bright unsaturated stars along with the best-fit curves. Then, adopting these best-fit curves as the PSF templates, every unsaturated star is masked with a circle with the radius where the count level is equal to  $1/10 \sigma$  of the local background count level. On the other hand, the saturated stars, magnitudes of which are supposed to be underestimated, are masked with a sufficiently large radius such as five or ten times larger than the expectation from the PSF templates. The unmasked and masked images are presented in Figure 2.5 and Figure 2.6, respectively. The fractions of masked areas in  $B$ ,  $g$ ,  $V$ , and  $R$  images are 17%, 31%, 19%, and 35%, respectively.

### 2.2.4 Aperture correction

In flux-scaling of the surface brightness of extended sources, as extensively discussed by Bernstein et al. (2002) and Mattila (2003), we have to take account of the effect to compensate a fraction of fluxes that scattered and diffracted into the aperture. Here we introduce the aperture correction factor  $T_A$ , which is the fraction of the flux from a point source within the aperture. In photometry of a point source, the flux from the point source

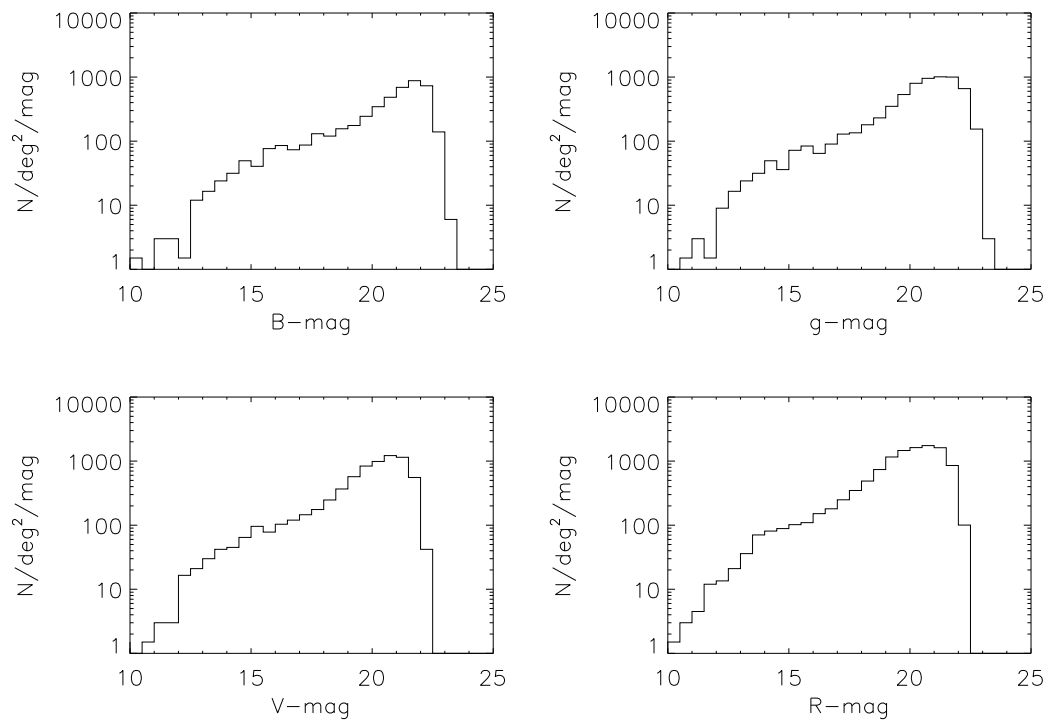


Figure 2.3 Histogram of the number of detected sources as a function of magnitude in 1 mag bins. Clockwise from upper-left: for  $B$ ,  $g$ ,  $V$ , and  $R$  band.

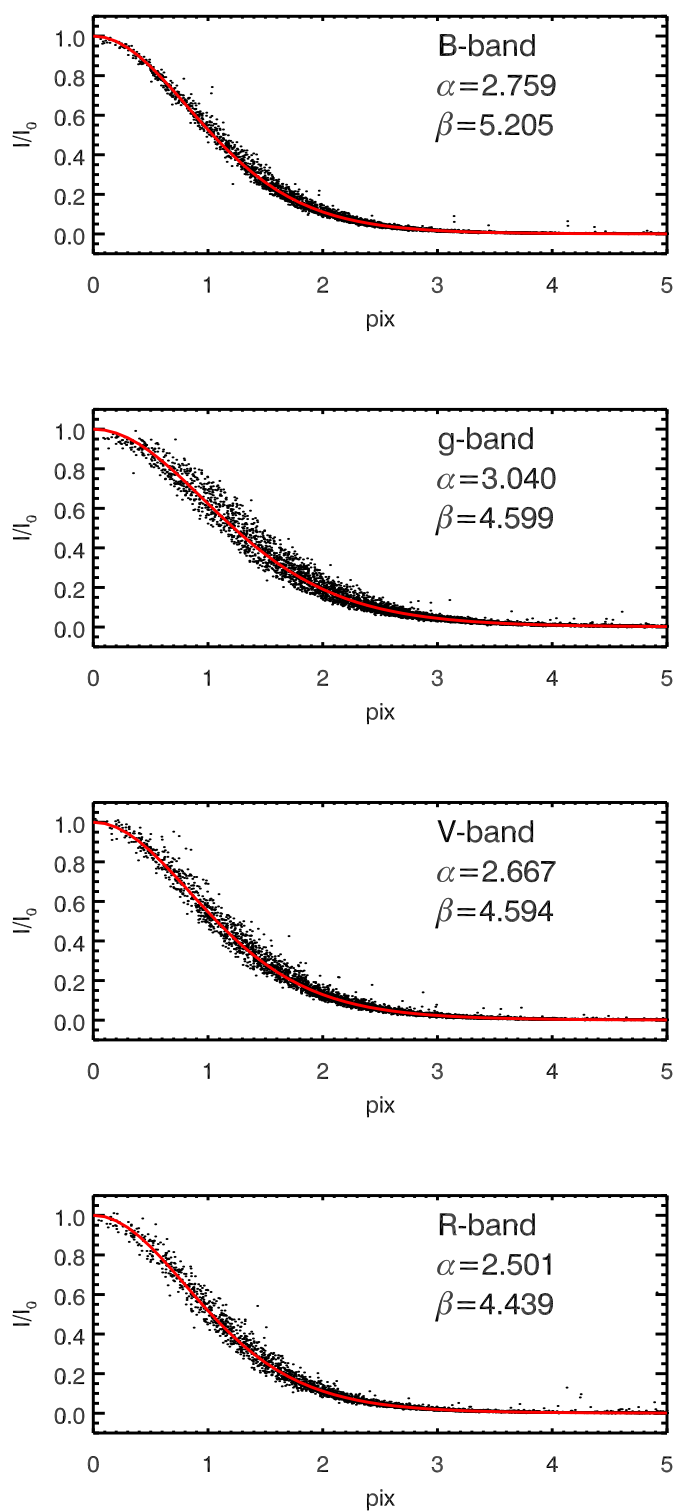


Figure 2.4 The scaled radial profiles of stellar images. Dots represent normalized fluxes of approximately hundred stars for each band. The red lines are the best fit of Moffat function;  $I = I_0[1 + (r/\alpha)^{-2}]^{-\beta}$ .

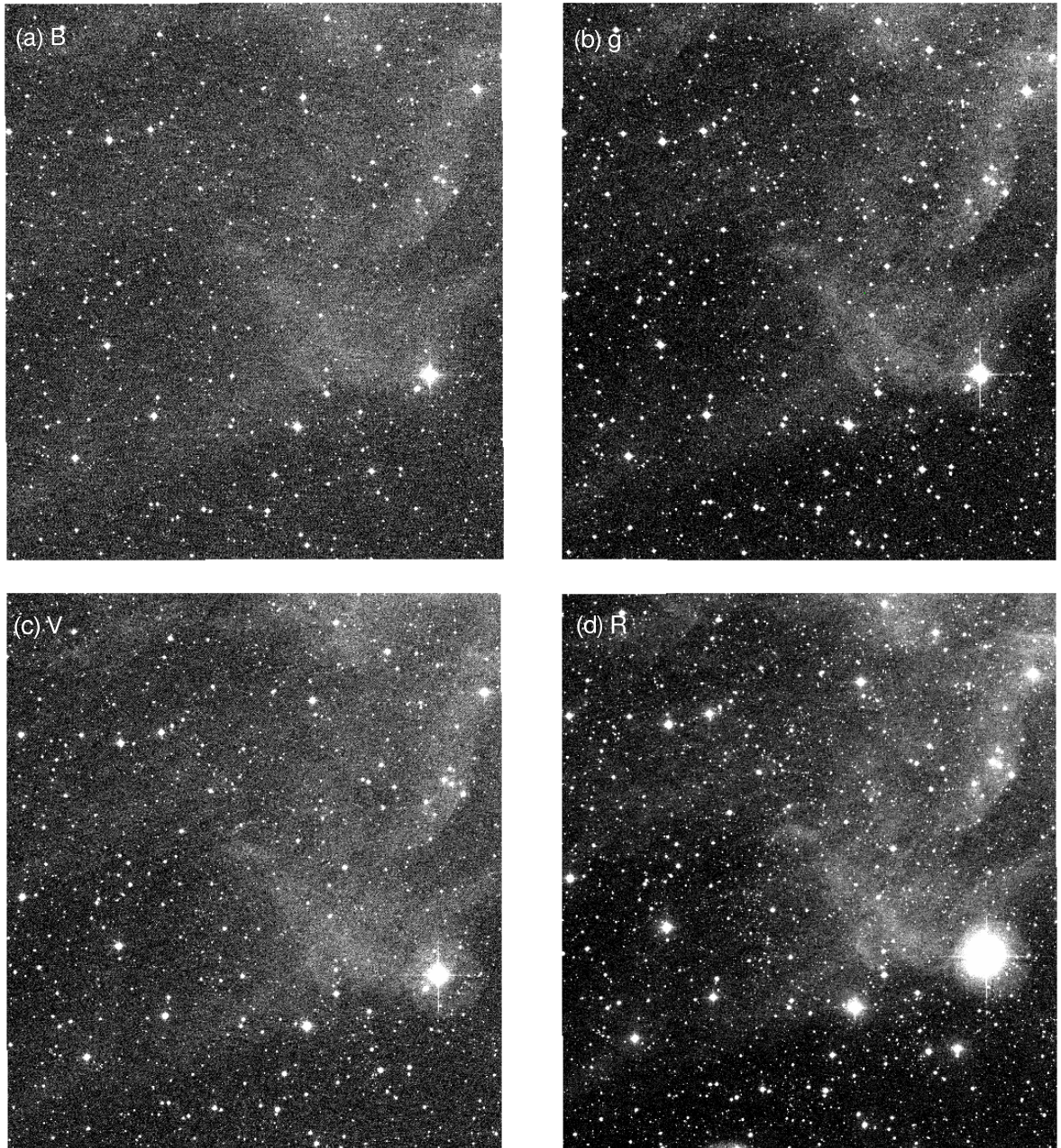


Figure 2.5 The optical images in *B*-band (a), *g*-band (b), *V*-band (c), and *R*-band (d). North is up, east to the left. The field is approximately  $45' \times 40'$ , slightly narrowed from the field of view of instrument due to the dithering.

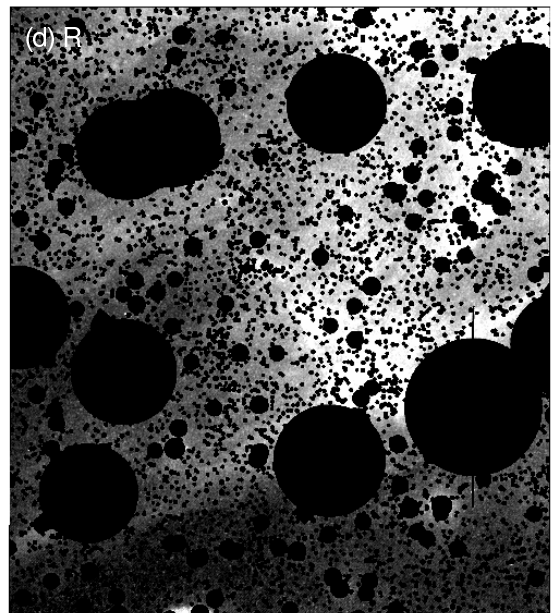
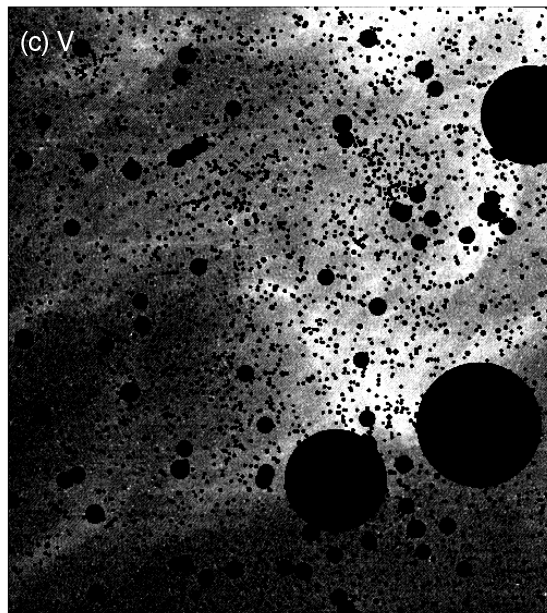
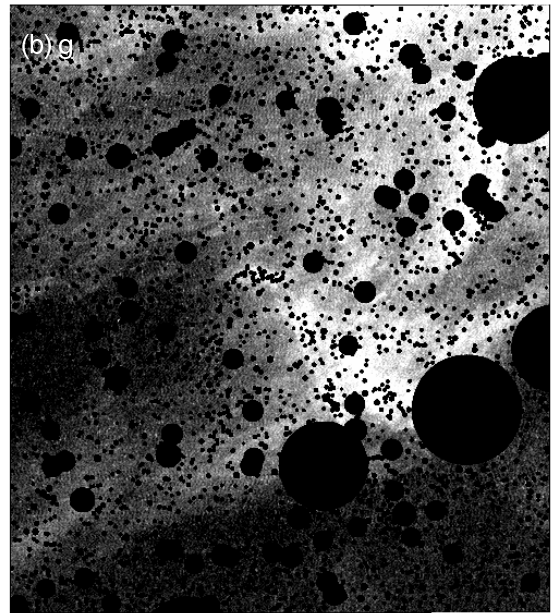
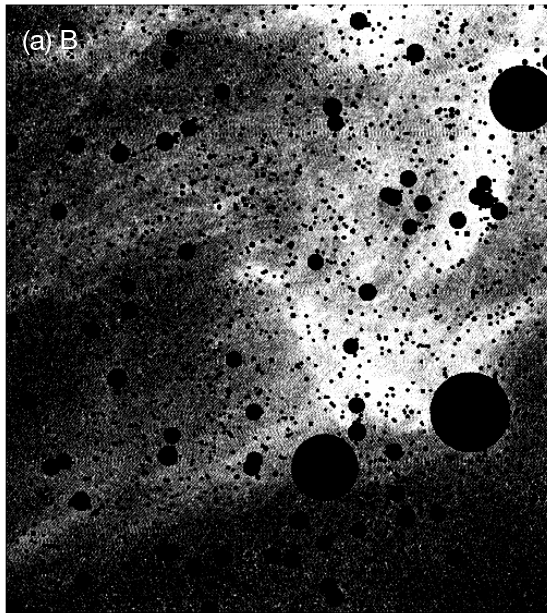


Figure 2.6 Same as for Figure 3, but for the masked optical images.

$F(\lambda)$  in units of Jy is given by

$$F(\lambda) = \frac{Q(\lambda)}{T_A(\lambda)} C(\lambda), \quad (2.1)$$

where  $C(\lambda)$  is the signal counts within the aperture in instrumental units (ADU),  $Q(\lambda)$  the sensitivity function in units of Jy ADU<sup>-1</sup>. Because  $F(\lambda)$  is known and  $C(\lambda)$  is measured, we can only derive  $Q'(\lambda) = Q(\lambda) / T_A(\lambda)$ , but not  $Q(\lambda)$  and  $T_A(\lambda)$  independently. In case of extended sources, no fluxes are lost; the fluxes lost from the aperture  $1 - T_A(\lambda)$  is compensated for by those scattered from the outside of the aperture. Therefore, the brightness of the extended source  $S(\lambda)$  in units of Jy sr<sup>-1</sup> is simply given as

$$S(\lambda) = \frac{Q(\lambda)}{\Omega} C(\lambda) = \frac{Q'(\lambda) T_A(\lambda)}{\Omega} C(\lambda), \quad (2.2)$$

where  $\Omega$  is the solid angle of the aperture in units of steradians. In the above equation,  $S(\lambda)$  is obtained once  $T_A(\lambda)$  is given.

The flux loss calculated from the measured PSF is negligible;  $T_A(\lambda) = 0.994$ . However, King (1971) pointed out that outside the central part of the profile, which is represented by a Gaussian or Moffat function, there is a more slowly declining halo or aureole. The aureole has a profile of an inverse-square law that extends over the central part by a factor of 1000 in angular distance, and contains about 5% of the star's light. Similar results are presented by several authors (Mattila 2003 and references therein). Even higher aureole energy fractions of  $\sim 10\%$  are reported in some cases (Capaccioli & de Vaucouleurs 1983; Uson et al. 1991). Here, we adopt the aperture correction factor  $T_A = 0.95 \pm 0.05$ .

### 2.2.5 Reducing the resolution

In order to compare the optical data and the far-IR data, we reduced the resolution of the optical images to the same resolution as the *IRAS*/DIRBE 100 $\mu$ m map ( $2'.372 \times 2'.372$ ) by averaging approximately 9,000 optical pixels. The resolution of the *IRAS*/DIRBE 100 $\mu$ m map is approximately 100 times lower than the optical seeing size. Therefore, in the course of the smoothing, the optical measurement errors are reduced due to the averaging of 9,000 independent data points. The mean one  $\sigma$  error per smoothed pixels  $\sigma(\lambda)$  in  $S_\nu(\lambda)$  of the smoothed star-masked images are summarized in Table 2.1. Finally, we obtained 385, 336, 384, 309 independent data points at  $B, g, V,$  and  $R,$  respectively.

### 2.2.6 Zodiacal light subtraction

The most recent map of the zodiacal light in the optical is based on the observation by Levasseur-Regourd & Dumont (1980). However, the resolution of that map is  $5^\circ$  and it is not suitable to estimate the spatial variations within the small area  $\sim 1^\circ \times 1^\circ$ . On the other

hand, in the infrared, relatively accurate maps were obtained by the DIRBE experiment on satellite COBE from  $1.24\mu\text{m}$  to  $240\mu\text{m}$ , and zodiacal light model was provided by Kelsall et al. (1998). This model was obtained by fitting the time variation of DIRBE all-sky observations over 10 months with a parametrized model of the dust cloud. As we can see in the figure 2.7, the structure of the zodiacal light in the optical and infrared are similar. Therefore we used this infrared zodiacal light model to predict the brightness of the optical zodiacal light in the observed field.

First, the zodiacal light at  $1.25\mu\text{m}$  were calculated for each pixel of the *IRAS*/DIRBE  $100\mu\text{m}$  map. Since the viewing direction respect to the sun, or  $\lambda - \lambda_{\odot}$ , differs by the date of observation, calculation has performed for each band. Then, the absolute brightness at  $1.25\mu\text{m}$  on each points were converted to brightness at the optical bands using the color conversion factors listed in Table 2.2. These conversion factors are obtained by interpolating the ratios of the brightness at each band to that of  $1.25\mu\text{m}$  in the table 1.1. Finally, calculated optical zodiacal light brightness were subtracted. The estimated variation of the zodiacal light within the observed field was very small ( $< 1 \text{ kJy sr}^{-1}$ ) at all bands, and even if the variation is twice larger than this estimation, that has little effect on following analysis or results. The absolute brightness of the Zodiacal light in each optical band is summarized along with the other components in Table 2.3 .

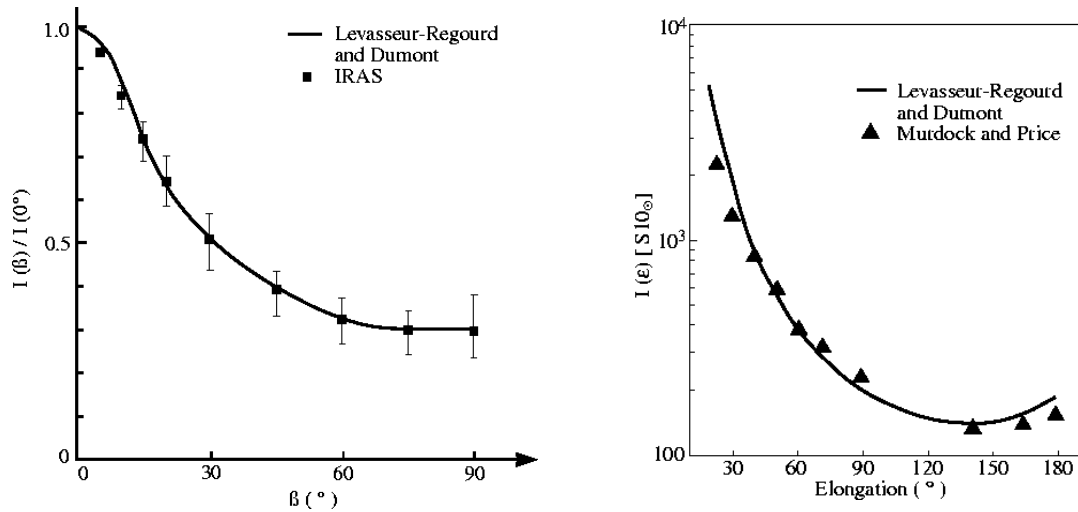


Figure 2.7 Comparison of the optical and infrared zodiacal light. Taken from Leinert et al. (1998). *Left panel:* Comparison of the out-of-ecliptic decrease of zodiacal light brightness at elongation from the Sun of  $90^\circ$  as measured from ground at  $502\text{ nm}$  (Levasseur-Regourd & Dumont 1980) and by IRAS (Vrtilek & Hauser 1995). The IRAS measurements are represented here by their annual average. The squares give the average of the profiles at  $12\mu\text{m}$ ,  $25\mu\text{m}$  and  $60\mu\text{m}$ , the bars given with the IRAS measurements show the range covered by the profiles at the different wavelengths, with the measurements at  $60\mu\text{m}$  delineating the lower and the measurements at  $12\mu\text{m}$  the upper envelope. All measurements are scaled by dividing the brightness at  $\beta = 0^\circ$ . *Right panel:* Comparison of zodiacal light brightness profile along the ecliptic as measured by (Levasseur-Regourd & Dumont 1980) at  $502\text{ nm}$  and by a rocket flight (Murdock & Price 1985) at  $10.9\ \mu\text{m}$  and  $20.9\ \mu\text{m}$ . The rocket data for the two wavelength bands have been averaged and normalized to the ground-based measurements at an elongation from the Sun of  $60^\circ$ .  $1[S10_\odot] = 1.28 \times 10^{-9} [\text{erg cm}^{-2} \text{ s}^{-1} \text{ sr}^{-1} \text{ \AA}^{-1}]$ .

Table 2.2 Conversion factors

Band	$\lambda_{center}$ ( $\mu\text{m}$ )	$C(\lambda)^\dagger$
<i>B</i>	0.44	0.42
<i>g</i>	0.49	0.53
<i>V</i>	0.55	0.71
<i>R</i>	0.65	0.78

$^\dagger$ Conversion factor:  $I_\nu(\lambda) = C(\lambda)I_\nu(1.25\mu\text{m})$

Table 2.3 Absolute brightness of the each component

Component	Contribution			
	<i>B</i> (kJy sr <sup>-1</sup> )	<i>g</i> (kJy sr <sup>-1</sup> )	<i>V</i> (kJy sr <sup>-1</sup> )	<i>R</i> (kJy sr <sup>-1</sup> )
Airglow <sup>†</sup>	140	220	490	360
Zodiacal light	50	80	90	100
DGL	10	13	24	21

$^\dagger$ Including any constant components, such as the EBL.

## Chapter 3

# Analysis and Results

Figure 3.1 plots the intensity of diffuse optical light  $S_\nu(\lambda)$  as a function of  $100\mu\text{m}$  intensity  $S_\nu(100\mu\text{m})$ .  $S_\nu(100\mu\text{m})$  is taken from the *IRAS/DIRBE*  $100\mu\text{m}$  map where the zodiacal light, stars, and galaxies are subtracted. Figure 3.1 shows that  $S_\nu(\lambda)$  clearly correlates with  $S_\nu(100\mu\text{m})$  at all the bands. We now fit to the data a linear function defined as:

$$S_\nu(\lambda) = a(\lambda) + b(\lambda)S_\nu(100\mu\text{m}) \quad (3.1)$$

where the slope parameter at wavelength  $\lambda$  is  $b(\lambda) = \Delta S_\nu(\lambda)/\Delta S_\nu(100\mu\text{m})$ , and the constant parameter  $a(\lambda)$  represents components independent of the Galactic diffuse optical light, i.e., atmospheric airglow, and any other light such as the EBL. Note that  $\lambda$  is *B*, *g*, *V*, or *R* for our broadband system, and  $a(\lambda), b(\lambda) > 0$ .

To perform a minimum  $\chi^2$  analysis with the effective variance method (Orear 1982), which can take into account both x and y errors, we need to know the standard deviation  $\sigma(100\mu\text{m})$  which are not explicitly estimated by SFD98. We thus carried out simulations by generating noiseless data points which follow equation (3.1) with given  $a(\lambda)$  and  $b(\lambda)$ , and adding Gaussian random errors to these points. The noiseless  $100\mu\text{m}$  data range from  $\text{MIN}(100\mu\text{m})$  to  $8 \text{ MJy sr}^{-1}$  with a frequency distribution  $\propto S_\nu(100\mu\text{m})^{-n}$ . At the low intensity end of  $S_\nu(\lambda)$  in Figure 3.1, the correlation appears to be truncated suddenly because of the large scatter of the  $100\mu\text{m}$  data. The center of the truncated boundary along the  $S_\nu(100\mu\text{m})$  axis is located around  $1.8 \text{ MJy sr}^{-1}$ . So, we set  $\text{MIN}(100\mu\text{m}) = 1.8 \text{ MJy sr}^{-1}$ . This was confirmed and justified by changing  $\text{MIN}(100\mu\text{m})$  in the simulations. While  $\sigma(\lambda)$  is taken from Table 2.1,  $\sigma(100\mu\text{m})$  is a parameter to be determined in the simulations. As shown in Figure 3.2, we find that a combination of  $n = 2$  and  $\sigma(100\mu\text{m}) = 0.3 - 0.4 \text{ MJy sr}^{-1}$  reasonably reproduces the correlation and the frequency distribution as a function of  $S_\nu(100\mu\text{m})$ . The left panel of the figure 3.2 shows the simulated data at *g*-band along with the linear function recovered from the  $\chi^2$  minimum analysis as well as the assumed linear

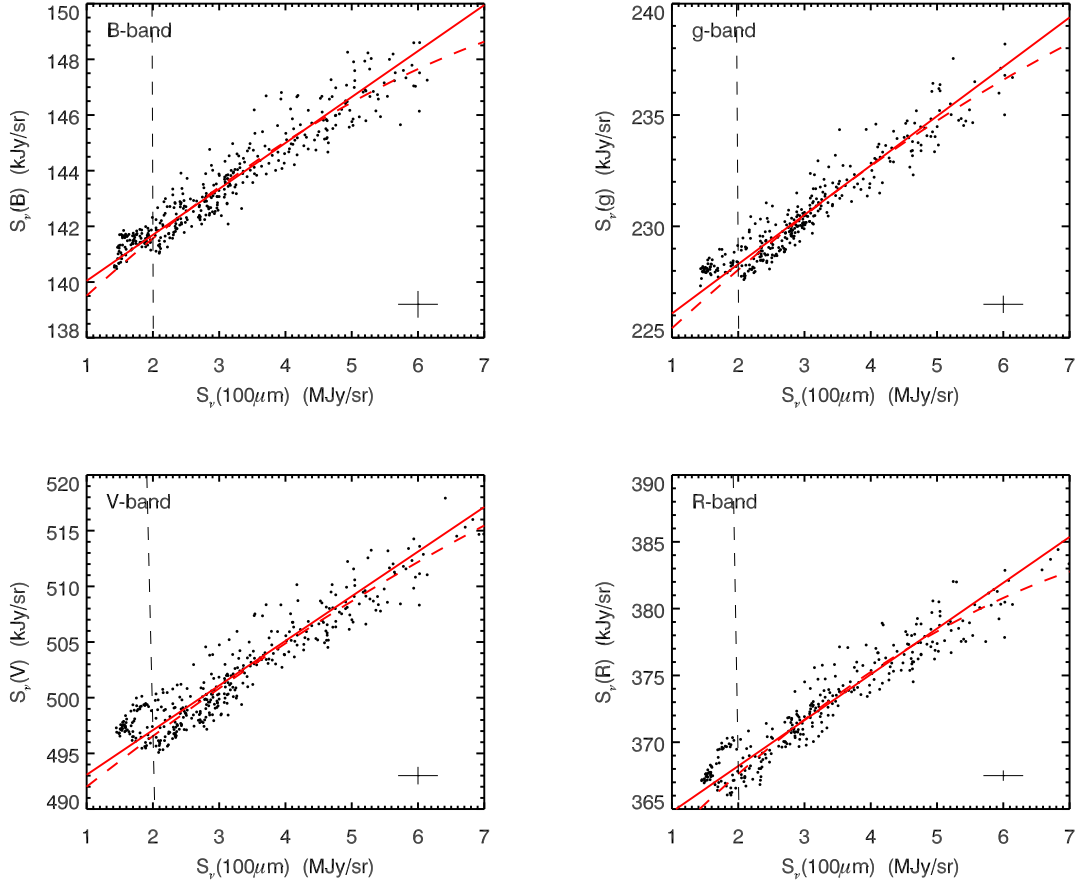


Figure 3.1 Correlation of the intensity of the diffuse optical light against  $100\mu\text{m}$  intensity. The red solid lines represent the linear functions recovered from the  $\chi^2$  minimum analysis, while the red dashed lines the quadratic functions. In case of a quadratic function, the fit is limited to the data points with  $S_\nu(100\mu\text{m}) \geq 2.0 \text{ MJy sr}^{-1}$  (right to the vertical dash line); all the data point are used to fit a linear function. The cross at lower left on each panel means the measurement error for each data points.

function to generate the mock data points.

Figure 3.1 plots the observed data along with the recovered linear function.  $a(\lambda)$  and  $b(\lambda)$  are listed in Table 3.1.

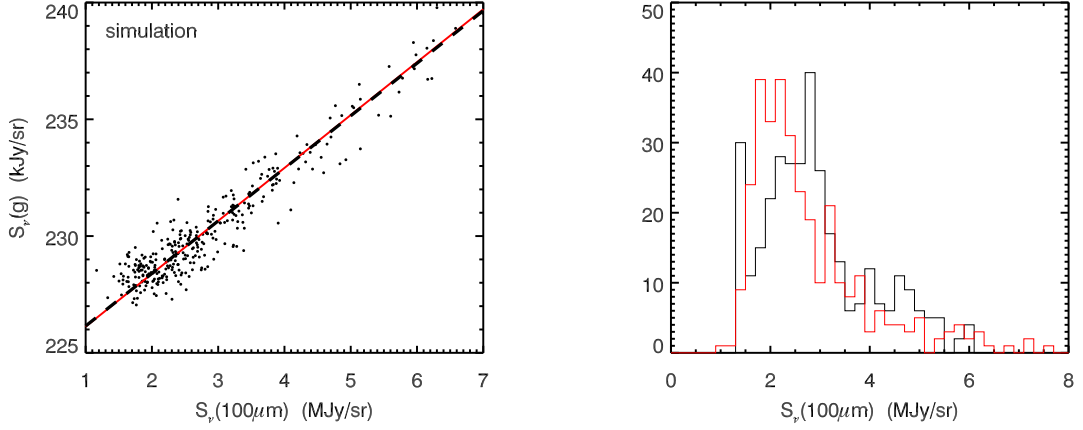


Figure 3.2 The *left* panel shows the simulated data at *g*-band along with the linear function recovered from the  $\chi^2$  minimum analysis as well as the assumed linear function to generate the mock data points. The dashed line represents the linear function assumed in the simulations, while the red line the recovered function. The *right* panel shows histogram of the observed (*black*) and generated mock data points (*red*).

Table 3.1 DGL model parameters.

Band	$S_\nu(\lambda) = a(\lambda) + b(\lambda)S_\nu(100\mu\text{m})$		$S_\nu(\lambda) = a^Q(\lambda) + b^Q(\lambda)S_\nu(100\mu\text{m}) + c^Q(\lambda)S_\nu(100\mu\text{m})^2$		
	$a(\lambda)$ (kJy sr $^{-1}$ )	$b(\lambda)$ ( $\times 10^{-3}$ )	$a^Q(\lambda)$ (kJy sr $^{-1}$ )	$b^Q(\lambda)$ ( $\times 10^{-3}$ )	$c^Q(\lambda)$ ([kJy sr $^{-1}$ ] $^{-1} \times 10^{-6}$ )
<i>B</i>	$138.39 \pm 0.12$	$1.65 \pm 0.11$	$137.24 \pm 0.46$	$2.38 \pm 0.25$	$-0.11 \pm 0.03$
<i>g</i>	$223.87 \pm 0.16$	$2.22 \pm 0.14$	$222.60 \pm 0.57$	$2.91 \pm 0.32$	$-0.10 \pm 0.04$
<i>V</i>	$489.07 \pm 0.46$	$4.01 \pm 0.28$	$487.21 \pm 0.97$	$4.92 \pm 0.52$	$-0.13 \pm 0.06$
<i>R</i>	$361.36 \pm 0.22$	$3.42 \pm 0.21$	$357.88 \pm 0.87$	$5.39 \pm 0.45$	$-0.26 \pm 0.06$

# Chapter 4

## Discussion

To discuss the new results in the context of a variety of similar result, we compiled  $b(\lambda)$  values, which are derived by fitting a liner function to observed correlation between optical and far-IR measurements, from the literature in a sample which is given in Table 4.1. Figure 4.1 compares the data in this sample with model predictions. The *IRAS*/DIRDE 100  $\mu\text{m}$  maps are used in Witt et al. (2008), Matsuoka et al. (2011), Brandt & Draine (2012), and ours, while early work namely Laureijs et al. (1987) used the original *IRAS* 100  $\mu\text{m}$  maps. The optical data are a collection of heterogeneous samples which were taken with different techniques and analyzed on different methods (see also Section 1.2). The broadband data taken from the literature are: fields towards high Galactic latitude cloud Lynds 1642 at 4700Å studied by Laureijs et al. (1987), and four high Galactic latitude clouds (MBM 30, 32, 41A, and 41D) at  $B$ ,  $G$ ,  $R$ , and  $I$  by Witt et al. (2008). The data studied by Matsuoka et al. (2011) were taken beyond the zodiacal dust cloud with the *Pioneer 10/11* Imaging Photopolarimeter(IPP) at  $B$  and  $R$  in regions with  $S_\nu(100\mu\text{m}) \leq 3 \text{ MJy sr}^{-1}$  at latitude  $|b| > 35^\circ$ , covering about a quarter of the whole sky. The spectrum by Brandt & Draine (2012), labelled "Full Sky Continuum" in their Figure 3, are obtained by analyzing the optical spectra of nearly 90,000 blank-sky spectra from the Sloan Digital Sky Survey (SDSS). Their spectrum has large uncertainty in the flux-scaling due to the analyzing method. The spectrum plotted in Figure 4.1 are scaled with their preferred bias factor of 2.1.

Our results are the first example which shows the spectra of  $b(\lambda)$  value for an individual cloud. The result of Laureijs et al. (1987) and our results, which are both derived from an individual cloud, are consistent with each other within error bars and our error bars are much smaller than that of Laureijs et al. (1987). The error bar on the measurement by Witt et al. (2008) is no greater than ours, but they do not take into account the systematical error such as the flux calibration error and aperture correction error. In fact, as you can

see in Figure 1.12 and Figure 3.1, our measurement error for each data points of the optical surface brightness is 6 times smaller than that of Witt et al. (2008) and the number of data points are about 5 times larger. For the results of Matsuoka et al. (2011) and Brandt & Draine (2012), the small error bar is due to their large number of data points, and their results shows an average values and errors of average of  $b(\lambda)$  in whole observed fields.

The reason why some observations, such as Guhathakurta & Tyson (1989) and Zagury et al. (1999), could not find clear correlations across their observed clouds may be an inaccurate flat-fielding. Because the results of Zagury et al. (1999) indicating that within narrow regions, about 1/10 of their observational field of view, where the effect of flat-fielding error would remain small and inconspicuous, their optical measurements and far-IR is well correlated.

## 4.1 Variations in slope parameter $b(\lambda)$

As can be seen in Figure 4.1,  $b(\lambda)$  varies by a factor of 2. In this subsections, we explore possible causes of the  $b(\lambda)$  scatter by examining the effects of optical depth, dust albedo, dust temperature and the forward-scattering characteristic of dust grains coupled to the non-isotropic interstellar radiation field(ISRF).

### 4.1.1 Optical depth and dust albedo

The correlation in Figure 3.1 may appear to be linear. However, as we discuss below, the linear correlation would not be expected in the case where the optically thin limit is not applicable, and significant changes in the optical depth along the sightline would cause large variations in  $b(\lambda)$ .

Figure 4.2 depicts  $b(\lambda)$  as a function of  $S_\nu^{ave}(100\mu\text{m})$  in two ranges of the effective broadband wavelengths, namely the blue range(0.44 - 0.46  $\mu\text{m}$ ) and the red range (0.64 - 0.66  $\mu\text{m}$ ).  $S_\nu^{ave}(100\mu\text{m})$  refers to the representative average of the lowest and highest values of the  $S_\nu(100\mu\text{m})$  range in which  $b(\lambda)$  are derived by assuming a linear function. The figure appears to show that the  $b(\lambda)$  decreases as  $S_\nu^{ave}(100\mu\text{m})$  increases, indicating that a significant portion of the reason for the large  $b(\lambda)$  scatter seen in Figure 4.1 can be attributed to this  $b(\lambda)$  -  $S_\nu^{ave}(100\mu\text{m})$  anti-correlation.

Accordingly we propose a correction to equation (3.1) as  $b(\lambda) = b^0(\lambda) + b^1(\lambda)S_\nu(100\mu\text{m})$ , or  $S_\nu(\lambda) = a(\lambda) + [b^0(\lambda) + b^1(\lambda)S_\nu(100\mu\text{m})]S_\nu(100\mu\text{m})$ . Then,  $S_\nu(\lambda)$  has a quadratic term as follows:

$$S_\nu(\lambda) = a^Q(\lambda) + b^Q(\lambda)S_\nu(100\mu\text{m}) + c^Q(\lambda)S_\nu(100\mu\text{m})^2, \quad (4.1)$$

Table 4.1 Correlation slopes  $b(\lambda)$  for high-latitude clouds or fields.

Reference Clouds or fields	$b(\lambda)^\dagger$ ( $\times 10^{-3}$ )	$\lambda_{center}$ ( $\mu\text{m}$ )	$S_\nu(100\mu\text{m})$ range $^\ddagger$ (MJy sr $^{-1}$ )	$b(R)/b(B)$
This work				
MBM32	$1.6 \pm 0.1$	0.44	1 - 7	2.1
	$2.3 \pm 0.1$	0.49		
	$4.0 \pm 0.3$	0.55		
	$3.4 \pm 0.2$	0.65		
Laureijs et al. 1987				
Lynds1642	$2.2 \pm 0.3$	0.47	1 - 13	
Witt et al. 1999				
Derived from 4 clouds	$2.1 \pm 0.1$	0.46	1 - 8	(2.0)*
Matsuoka et al. 2011				
1/4 of the entire sky ( $ b  > 35^\circ$ )	$2.1 \pm 0.1$	0.44	1 - 3	2.2
	$4.6 \pm 0.1$	0.64		
Brandt et al. 2012				
90,000 SDSS spectra	$1.2 \pm 0.1$	0.45	1 - 10	1.9
	$1.9 \pm 0.1$	0.55		
	$2.3 \pm 0.1$	0.65		
	$2.4 \pm 0.1$	0.80		

$^\dagger$ The correlation slope is defined as a linear function of  $S_\nu(\lambda) = a(\lambda) + b(\lambda)S_\nu(100\mu\text{m})$

$^\ddagger$  $S_\nu(100\mu\text{m})$  range refers to the range in which  $b(\lambda)$  is derived assuming a linear function.

\*This value does not represent  $b(R)/b(B)$ , but  $S_\nu(R)/S_\nu(B)$ .

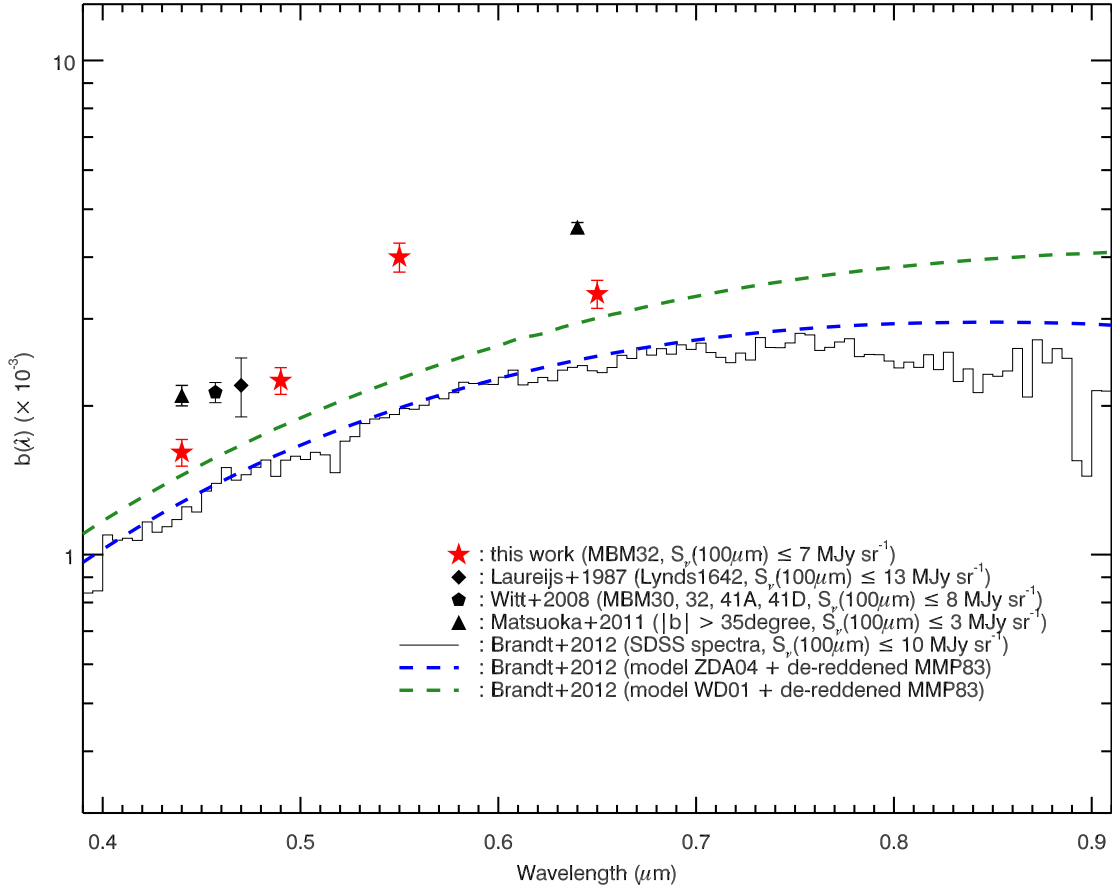


Figure 4.1 The correlation slopes  $b(\lambda) = \Delta S_\nu(\lambda)/\Delta S_\nu(100\mu\text{m})$  as a function of wavelengths.

where  $b^Q(\lambda) > 0$  and  $c^Q(\lambda) < 0$ . While the correlation in Figure 3.1 appears to be linear, the actual fact is that the correlation is non-linear, but this is hidden by the prevailing noise. Since the quadratic term  $c^Q(\lambda)S_\nu(100\mu\text{m})^2$  is negative, this would explain why the correlation of the *Pioneer* data deviates below the best-fit linear function at the bright end of  $100\mu\text{m}$  emission (Matsuoka et al. 2011). We performed a minimum  $\chi^2$  analysis with the effective variance method to fit the quadratic function to our data. As can be seen in Table 3.1 and Figure 3.1, the derived constant parameter of a quadratic function  $a^Q(\lambda)$  is smaller than that of a linear function  $a(\lambda)$  at all the photometric bands. Thus, this negative quadratic term would be important for the separation of the COB from the diffuse optical light, reducing the DGL intensity at which  $S_\nu(100\mu\text{m})$  is equal to the Cosmic  $100\mu\text{m}$  background intensity.

The origin of the quadratic term could be attributed to the fact that our sample directions are not optically thin, but translucent or thick. Witt et al. (2008) conclude, after reviewing a wide range of available data in the literature that, a ration of  $100\mu\text{m}$  intensity to visual extinction  $S_\nu(100\mu\text{m})/A_V$  is about  $10 \text{ MJy sr}^{-1} \text{ mag}^{-1}$ . for high-latitude diffuse clouds. Our sample ranges from  $S_\nu(100\mu\text{m}) = 1$  to  $13 \text{ MJy sr}^{-1}$ , corresponding  $A_V = 0.1 - 1.3 \text{ mag}$ . Thus, dust absorption along the sightline should be taken into account.

To illustrate the effect of extinction along the sightline, as fully discussed in the Appendix, we consider a simple model where a plane-parallel dust slab is illuminated by the monochromatic starlight from the backs. The  $b(\lambda)$  is expressed as

$$b(\lambda) \propto \exp[-(1 - \omega)\tau][1 - \exp(-\omega\tau)]/\{1 - \exp[-(1 - \omega)\tau]\}, \quad (4.2)$$

where  $\omega$  is the albedo, and  $\tau$  is the optical depth of the cloud.

Equation (4.2) implies that  $b(\lambda)$  depends on the optical depth and the albedo, but not to the ISRF intensity. In Figure 4.2, we plot equation (4.2) with a constant value of proportionality  $X^1$  for top and middle panels, assuming  $S_\nu(100\mu\text{m})/A_V = 10 \text{ MJy sr}^{-1} \text{ mag}^{-1}$ .  $X$  is set to the appropriate value by eyes for each panel independently. The three lines depict the relation for albedo at  $V$ ,  $\omega_V$  of 0.6, 0.7, and 0.8 from bottom to top. Figure 4.2 suggests that a range of  $A_V = 0.1 - 1.3 \text{ mag}$  could change the  $b(\lambda)$  strength by a factor of  $\sim 2$  while keeping  $\omega$  constant. The relation between  $b(\lambda)$  and  $S_\nu(100\mu\text{m})$  is not simple, since  $b(\lambda)$  in equation (4.2) is not linearly related to  $\tau$  and  $S_\nu(100\mu\text{m})/A_V$  has some uncertainty. However as seen in Figure 4.2, the relation between  $b(\lambda)$  and  $S_\nu(100\mu\text{m})$  is not far from a linear relation. This is why we approximate the relation as  $b(\lambda) = b^0(\lambda) + b^1(\lambda)S_\nu(100\mu\text{m})$ .

---

<sup>1</sup> $b(\lambda) = X \exp[-(1 - \omega)\tau][1 - \exp(-\omega\tau)]/\{1 - \exp[-(1 - \omega)\tau]\}$

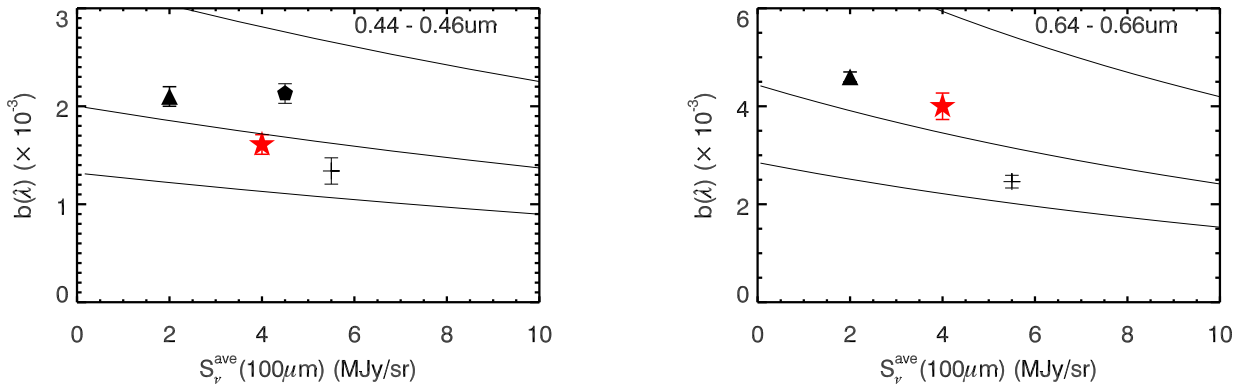


Figure 4.2 The *left* panel plots the correlation slopes  $b(\lambda)$  as a function of  $S_{\nu}^{ave}(100\mu\text{m})$  for the blue range (0.44 to 0.46  $\mu\text{m}$ ).  $S_{\nu}^{ave}(100\mu\text{m})$  refers to the representative average of the lowest and highest values of the  $S_{\nu}(100\mu\text{m})$  range in which  $b(\lambda)$  is derived by fitting a linear function. Spectroscopic data are averaged over this range. The *right* panel is the same as for the *left* panel but for the red range (0.64 to 0.66  $\mu\text{m}$ ). The legend for the points is the same as in Figure 4.1, except for the crosses which are the averaged spectroscopy data from Brandt & Draine (2012). The lines represent the relation expected from equation (4.2) for albedos  $\omega_V = 0.6, 0.7$ , and  $0.8$  from lower to upper.

#### 4.1.2 Dust Temperature

The surface brightness of the 100  $\mu\text{m}$  thermal radiation is usually expressed as a product of the optical depth at 100  $\mu\text{m}$  and the Planck function at the effective temperature of large dust grains. Thus, variations in the dust temperature are a possible cause of the large  $b(\lambda)$  scatter. It may seem that the increase of the temperature result in the increase of the 100  $\mu\text{m}$  emission and, as a result, decrease the  $b(\lambda)$ . However the real situation is not so simple. Because the temperature of the dust grain is determined by the balance between incoming energy from the illuminating radiation to the grain and the outgoing infrared thermal energy. In order to increase the temperature, the grain has to be illuminated by stronger ISRF and that also makes the DGL strong. Moreover, as Lehtinen et al. (2007) showed, the dust emissivity, measured by the ratio of far-infrared optical depth to visual extinction,  $\tau(\text{far} - \text{IR})/A_V$ , decreases as a function of dust temperature, and the higher temperature dust does not necessarily result in higher surface brightness at the 100  $\mu\text{m}$ . They concluded that the emissivity variations are caused by the variations in the absorption cross section of dust at far-IR, or the grain size distribution.

Since the observed  $b(\lambda)$  values other than ours are the average values of several clouds or very wide fields, we cannot discuss the temperature dependence from the observational results. Therefore, it is important to increase the sample of observations for individual

cloud like this thesis, in order to know how the dust temperature affects the correlation between optical and the far-IR. And also it is noted that *IRAS*/DIRBE temperature map which is widely used as an all sky dust temperature map is severely limited by the angular resolution of DIRBE of  $\sim 1$  degree. Thus, this map is not capable of correctly reflecting the temperature variations in cloud structures of angular extent of less than 1 degree such as the cloud observed in this thesis. In order to examine the dependence on the dust temperature, far-IR data with higher resolution are highly anticipated.

### 4.1.3 Latitude and longitude

Another possible cause of the large  $b(\lambda)$  scatter is the effect of the forward-scattering characteristic of dust grains. The ISRF is non-isotropic because of the stellar concentration toward the Galactic disk. The scattering efficiency in the direction towards the observer is coupled to this non-isotropy through the forward-scattering phase function of scattering grains. This effect is maximized for the geometric configuration explored by Jura (1979) and Stark (1995). The latitude dependence of surface brightness of a cloud at high latitude was studied, employing the Henyey & Greenstein (1941) approximation for the scattering phase function. In this model, it is assumed that a cloud is illuminated by an infinite homogeneous disk. The observer is located in the plane, and the cloud is located above the plane. The numerical results by Jura (1979) show that the surface brightness of a cloud  $S$  is written as

$$S \propto 1 - 1.1g\sqrt{\sin |b|} \quad (4.3)$$

where  $g$  is an asymmetry factor and  $b$  the Galactic latitude. For strong forward scattering,  $g \sim 1$ ; for isotropic scattering,  $g \sim 0$ . This equation shows that the brightness of the scattered light is significantly changed with the latitude of the cloud. Adopting a typical asymmetry factor  $g \sim 0.75$ , the intensity of the scattered light at  $b = 30^\circ$  is 2-3 times larger than that of at  $b = 90^\circ$ . This model assumes that all radiation sources ,i.e. stars, are located just in a plane, however, this is not the case. In fact, the mean vertical height of high-latitude clouds is  $\sim 150$  pc (Magnani et al. 1996) and that of stellar disk is  $\sim 300$  pc (Bahcall & Soneira 1980; Gilmore & Reid 1983). Thus, the geometry used in the model of Jura (1979) is extreme. It would be more natural to assume that a significant portion of stars are located behind the high-latitude clouds.

To examine the effectiveness of the forward-scattering characteristic of dust grains, we present Figure 4.3, illustrating  $b(\lambda)$  as a function of Galactic latitude  $|b|$  (*upper panels*) and longitude  $|l|$  (*lower panels*). There are no  $b(\lambda)$  dependency on both the latitude  $|b|$  and longitude  $|l|$  at all. For comparison, equation (4.3) with  $g = 0.75$  is plotted in upper panels

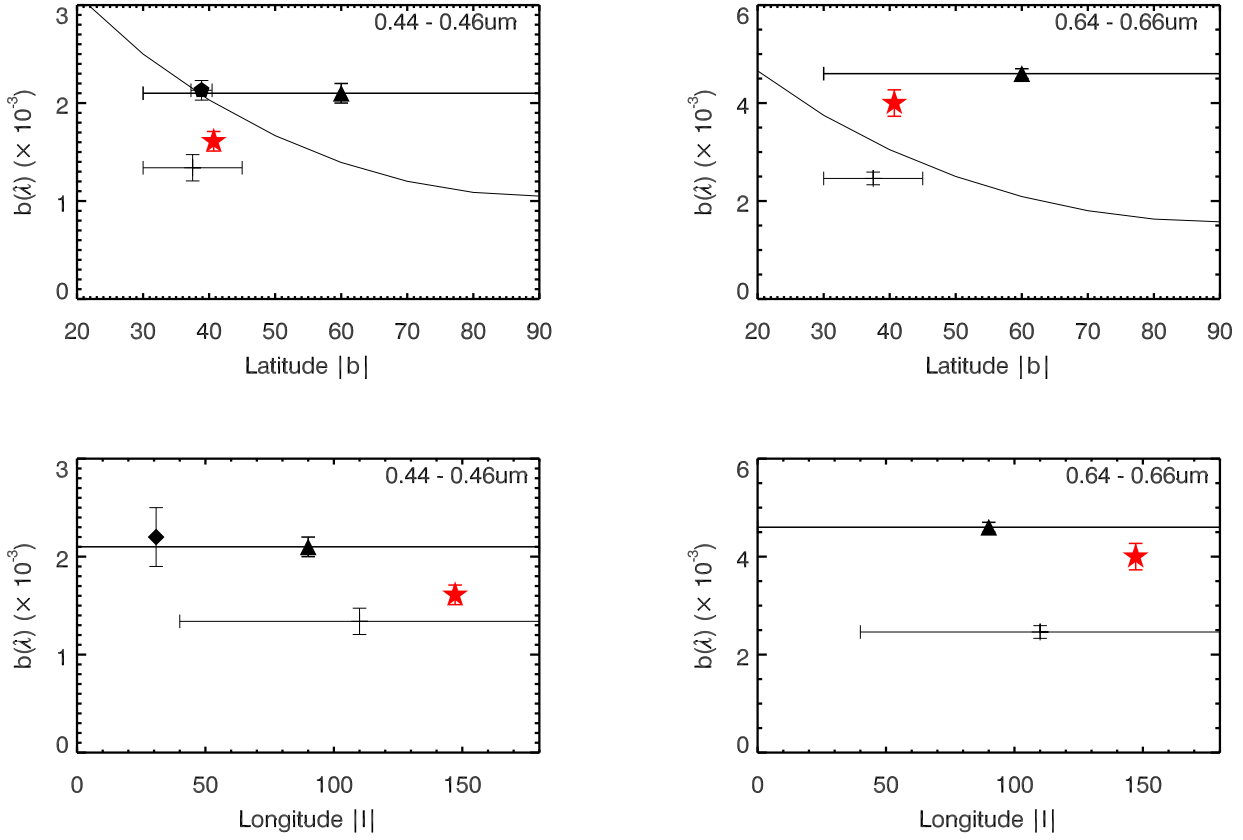


Figure 4.3 The *upper* panels plot the correlation slopes  $b(\lambda)$  as a function of latitude  $|b|$ , the *lower* panels the correlation slopes  $b(\lambda)$  as a function of longitude  $|l|$ . The *left* and *right* panels are for a range of the effective broadband wavelengths from 0.44 to 0.46  $\mu\text{m}$  and for a range from 0.64 to 0.66  $\mu\text{m}$  respectively. The legends are same as those in Figure 4.1. The horizontal error bars are represent their coordinate ranges.

of Figure 4.3. The absolute value of the equation is determined by eyes to fit the observed data. It appears that there are no  $b(\lambda)$  dependency on both the latitude  $|b|$  and longitude  $|l|$  at all. In order to examine the dependence on the latitude and longitude, the number of samples of observations for individual have to be increased.

## 4.2 Scattering Models

Two smooth curves in Figure 4.1 are synthesized spectra for  $\tau_V = 0.15$  by Brandt & Draine (2012), adopting the ISRF spectrum by Mathis et al. (1983) combined with a simple plane-parallel galaxy model and two dust models from Zubko et al. (2004) and Weingartner & Draine (2001) (hereafter ZDA04 and WD01 models). The models underestimate  $b(\lambda)$  by a factor of 2. There would be two possible explanations for this. One is deficient in UV photons compared to the assumed spectrum of the ISRF; the dust temperature is low and  $b(\lambda)$  thus increases where the dust grains are illuminated by a small number of UV photons (see Figures 9 and 10 in Brandt & Draine 2012). The other is that albedo is greater than assumed in the models, because Figure 4.2 and equation (4.2) imply that the  $b(\lambda)$  strength is doubled if  $\omega$  increases by 20%; for example,  $\omega_V$  to be 0.8 instead of a standard Milky Way value of 0.67 at V (Draine 2003). If this is the case, more large grains are needed than in the ZDA04 and WD01 models, because large grains are efficient scatterers of light.

### 4.2.1 Extended red emission

The extended red emission (ERE) is an emission from the interstellar dust grains in the 500-900 nm spectral range. It is thought that ERE is the result of an interaction of far-UV photons with interstellar dust (Witt & Schild 1985; Darbon et al. 1999; Witt et al. 2006). The ERE is observed in reflection nebulae (Witt et al. 1984; Witt & Schild 1988; Witt & Boroson 1990), HII regions (Perrin & Sivan 1992), and planetary nebulae (Furton & Witt 1990, 1992). However, in the diffuse interstellar medium, such as high latitude cloud, some authors favor the presence of the ERE in the diffuse optical light<sup>2</sup> (e.g., Guhathakurta & Tyson 1989; Gordon et al. 1998; Witt et al. 2008; Matsuoka et al. 2011), while the others suggest the absence of the ERE (Zagury et al. 1999; Zagury 2006) based on broadband observations. Carrying out spectroscopy of the diffuse optical light toward a high latitude cloud, Szomoru & Guhathakurta (1998) claimed to detect the ERE peaking at 6000Å, which is blue-shifted compared with 8000Å for HII regions and 7000Å for reflection nebulae and planetary nebulae. On the other hand, the more recent spectroscopic study by Brandt & Draine (2012) cannot find any evidence of the ERE.

There is some confusion in the DGL models, which are sometimes used for the claim of ERE detection; ERE is detected, if the observed diffuse optical light is redder than those predicted by the model, and vice versa. In Figure 4.4, we showed some model predictions along with our observational results. Here we introduce the  $b(R)/b(B)$  value, which is a

---

<sup>2</sup>In this section, we use the term “DGL” as the scattered component and “diffuse optical light” as the total optical component including the DGL and any other emissions.

measure of the redness of the diffuse optical light. As indicated in Table 4.1, measured  $b(R)/b(B)$  values are typically  $\sim 2$ . Models by Witt & Schild (1985), Guhathakurta & Tyson (1989), and Bernstein et al. (2002) predict  $b(R)/b(B) \sim 1.4$ , which is bluer than the measured values  $b(R)/b(B) \sim 2$ , supporting the presence of ERE in the diffuse optical light. Their models are basically same as a simple model where the optical surface brightness of the DGL is determined by multiplying the ISRF by the extinction cross-section of dust grains by the dust albedo. In contrast, Gordon et al. (1998) predicted  $b(R)/b(B) \sim 1.9$ , using the Witt-Petersohn DGL model (WP model; Witt & Petersohn 1994; Witt et al. 1997), an advanced Monte Carlo multiple scattering model utilizing the actual Galactic radiation field and realistic dust scattering properties. Brandt & Draine (2012) also predicted  $b(R)/b(B) \sim 1.9 - 2.0$  using their scattering DGL models (ZDA04 and WD01). These are consistent with the observed values without ERE.

It should be pointed out that our  $b(\lambda)$  in Figure 4.4 favors the ERE in the diffuse optical light;  $b(\lambda)$  rises from B to V faster than the models, seems to peak around 6000 Å and decreases towards long wavelengths. Such characteristic is expected from the models in which the scattered DGL combined with the ERE.

Another issue on the ERE observations is related to the optical depth of the ISM at far-UV. In the observations referred in this thesis, the surroundings of the high Galactic latitude clouds are optically thin at optical wavelengths. However, far-UV optical depth relevant for the excitation of ERE are at least 3.5 times larger than the corresponding optical depth at V-band and hence the surroundings will be quite optically thick. Thus, ERE can be excited only in clouds surface layers to an intensity that is similar to the ERE in the clouds surroundings. As a consequence, the ERE brightness is saturated across a much larger field than the optical DGL brightness. If the ERE brightness is saturated all over the observed field, contribution from the ERE would be included in constant parameter  $a(\lambda)$  in our analysis (see equation 3.1 in chapter 3). A solution to this problem is to measure the brightness or redness of diffuse optical light directly, i.e, not using  $b(R)/b(B)$ , but  $S_\nu(B)/S_\nu(R)$ . However, this is very difficult because we have to remove all the diffuse components other than the DGL and the ERE. Especially, in the observations like ours, the airglow and the zodiacal light is nearly constant over the field of view and these are indistinguishable from the ERE that is also constant over the field of view. Studies based on *Pioneer*10/11 data obtained outside the zodiacal cloud, i.e. Gordon et al. (1998) and Matsuoka et al. (2011), eliminate these difficulties, but if the constant EBL is existed, it is indistinguishable from the ERE. Another solution to the problem is to observe the fields that including areas the far-UV optical depth is thin. In these fields the brightness of the ERE would increase as the optical depth increasing and thus the analysis used in this thesis

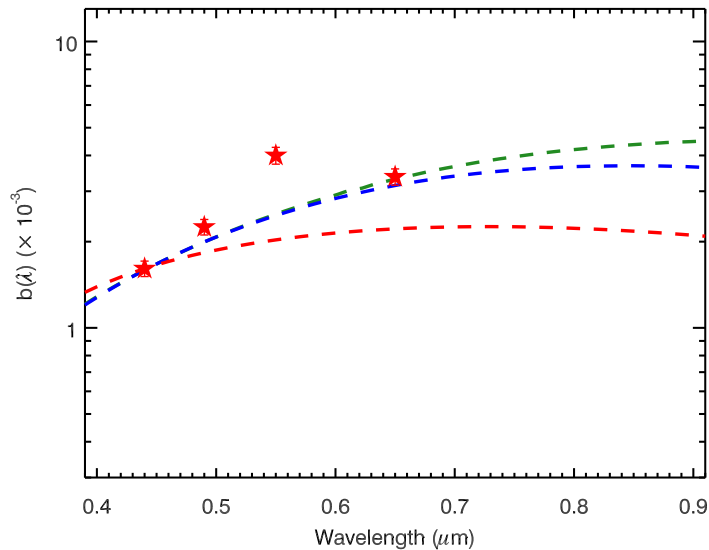


Figure 4.4 The spectra of the DGL models. Blue and green curves are the ZDA04 and WD01 models, respectively. Red curve is a simple model equivalent of the models by Witt & Schild (1985), Guhathakurta & Tyson (1989), and Bernstein et al. (2002). In this simple model the surface brightness of the DGL is determined by multiplying the ISRF by the extinction cross-section of dust grains by the dust albedo. The ISRF model by Mathis et al. (1983) and dust model by Draine (2003) are adopted. The absolute values of the models are scaled to our observed values at *B*-band.

is valid.

#### 4.2.2 DGL in the near infrared

In the near infrared, the DGL thought to be very weak and has heretofore been largely ignored. However, as you can see in Figure 4.4, the recent models (e.g. Brandt & Draine 2012) shows that the color of the DGL can be much redder than the simple models. Our results support the redder color of the DGL. If the redder models are correct, the surface brightness of the DGL in the near infrared would be stronger than previously thought. The observation of the DGL in the near infrared is very important for test of the scattering and dust models, and for background measurement in this wavelengths.

# Chapter 5

## Summary

We have conducted  $B$ ,  $g$ ,  $V$ , and  $R$ -band imaging in a  $45' \times 40'$  field containing part of high Galactic latitude translucent cloud MBM32, and correlated the intensity of diffuse optical light  $S_\nu(\lambda)$  with that of  $100 \mu\text{m}$  emission  $S_\nu(100\mu\text{m})$ . In the context of a variety of similar results taken from the literature, we discussed the scatter of the slope parameter  $b(\lambda) = \Delta S_\nu(\lambda)/\Delta S_\nu(100\mu\text{m})$  and the possible detection of extended red emission (ERE) through a comparison of the data with model predictions of the colors of the diffuse galactic light (DGL).

Detailed summary are as follows:

- We found excellent, near-linear correlations between the diffuse optical light and the  $100 \mu\text{m}$  brightness. A minimum  $\chi^2$  analysis is applied to fit a linear function to the measured correlation and derive the slope parameter  $b(\lambda)$  of  $(1.6 \pm 0.1) \times 10^3$ ,  $(2.2 \pm 0.1) \times 10^3$ ,  $(4.0 \pm 0.3) \times 10^3$ , and  $(3.4 \pm 0.2) \times 10^3$  at  $B$ ,  $g$ ,  $V$ , and  $R$ -band, respectively. Our results are the first example which shows the spectra of  $b(\lambda)$  value for an individual cloud.
- We evaluated the uncertainty caused as the result of removal of the foreground emission, such as the airglow, the zodiacal light, and the faint stars. These effects are not well considered or ignored in previous studies. We found that the effect of the variation of zodiacal light in small areas ( $\sim 1^\circ$ ) and the residual flux from the faint stars ( $\geq 20$  mag) are less than about 1/10 the DGL brightness, and these do not affect the derived slope parameter. On the other hand, large-scale non-uniformity of flat-fielding coupled with the brightest foreground emission, airglow, would cause a significant effect on derived slope parameter.
- In order to reduce the effects of large-scale non-uniformity of flat-fielding, we evaluate and calibrate the flat image by observing the same sky area by different positions of

the CCD and comparing the measured brightness. As a result we found that the error of the flat-fielding could be reduced to  $\sim 0.2\%$  per degree.

- On the course of deriving the slope parameter, we evaluated the error of the *IRAS*/DIRDE 100  $\mu\text{m}$  maps by simulating the scatter of the data points. The obtained error is 0.3-0.4 MJy/sr in our observed field.
- We compiled the slope parameter  $b(\lambda)$  from the literature in a sample, and found that these  $b(\lambda)$  values changes by factor of 2 in our sample. We explored the cause of this scatter from the aspects of optical depth through the line-of-sight, temperature of the dust, and the latitude of the observed fields. We found that the  $b(\lambda)$  decreases as the optical depth increasing. Using a simple radiative transfer model, we showed that the variations of optical depth along with the variations of dust albedo for each cloud can explain the scatter of  $b(\lambda)$ .
- We showed that the linear correlation between the diffuse optical light and the 100  $\mu\text{m}$  brightness is not expected in case that the optically thin limit is not applied. When the correlation is utilized for removing the DGL in order to measure the extragalactic background light, this non-linear term should be taken into account.
- As for the ERE, comparing the observations and several models, it would be fair to say that no models are accurate enough to reject or confirm the presence of the ERE in the diffuse interstellar medium, at this time. However, our  $b(\lambda)$  spectrum seems to peak around 6000  $\text{\AA}$  and decreases towards long wavelengths. Such characteristic is expected from the models in which the DGL combined with the ERE.

In order to comprehensively understand the DGL, progress of both optical and far-infrared observations is necessary. As for the optical observation, the accuracy of the measurement depends on how accurately remove the foreground diffuse components other than the DGL. Thus, observations from outside the zodiacal dust cloud is an ultimate way and ,in fact, such mission named Exo-Zodiacal Infrared Telescope (EXZIT) is planned. In ground-based observations, the major foreground is the airglow and, therefore, the accuracy of the flat-fielding is crucial. We cannot expect a significant improvement in the accuracy of the ground-based observation. However, in order to examine the dust temperature dependence or latitude and longitude dependence of  $b(\lambda)$ , it is important to increase the example of the observation for a individual cloud. As for the far-infrared observation, the infrared astronomical satellite *AKARI*/Far-infrared surveyor (FIS) performed an all sky survey at four infrared bands (65, 90, 140, and 160  $\mu\text{m}$ ), with  $\sim 1'$  resolution (Murakami et al. 2007),

which is much higher than that of the *IRAS*. The diffuse brightness maps constructed by *AKARI*'s data would make it possible to study the spatial structures and the temperature across the cloud. The observation of the DGL in near-infrared is also highly anticipated for test of the scattering and dust models, and for background measurement in this wavelengths.

# Appendix A

## Flat-fielding

Flat-fielding is a basic step to calibrate two-dimensional response of telescope-sensor systems. A source of uniform light is used to take a flat-field image (hereafter called simply flat image) which records differences in sensitivity across the field of view. Raw images that is to be used for scientific analysis (hereafter called raw science image) are corrected by divided by the flat image.

Dome, twilight, and night-sky flat images are frequently used for this purpose. Dome flat images are obtained by observing a screen illuminated by light sources inside the dome. Dome flat images can be easily obtained with a good signal to noise ratio in a short exposure, while scattering angles on the screen relative to the telescope can be changed during the night for various reasons such as inelastic flexure of the screen which can be induced by dome rotation or the rough control of the dome rotation angle.

Twilight flat images are obtained by observing the sky during evening or morning twilight. The twilight-sky better approximates the spectrum of astronomical objects than light sources of dome flat images. However, the twilight-sky brightness changes quickly, requiring a difficult task to change exposure times, because this process is not usually automated especially on small telescopes, and the scattering of light at the dome slit or the telescope structure may disturb the uniform illumination.

Night-sky flat images or self-flat images are obtained by employing sky data in raw science images. Raw science images are coadded by taking median means with ignoring the telescope pointing information. In this way, light from stars and galaxies are effectively removed from the coadded image. However, if the observed sky has some structure in brightness such as diffuse galactic light (DGL), this structure can not be removed completely and remains as an error in the generated flat image.

Whichever flat image is used, it is not unusual that a flat image has an artifactual gradient of roughly 1% per degree (Chromey & Hasselbacher 1996). In order to improve

the accuracy of flat fielding, stellar photometry is sometimes used to compare observed magnitudes and catalog magnitudes or compare observed magnitudes in shifted and rotated frames (Andersen et al. 1995; Manfroid 1995; Koch et al. 2004). Using stellar photometry, we may reach an accuracy of about 0.3% across the field of view. However, it will be time-consuming to reach such an accuracy.

In this chapter, we discuss dome-flat fielding to observe very extended diffuse objects like the DGL. Our goal is to reduce the large-scale ( $\sim 10' - 1^\circ$ ) non-uniformity of dome flat image, such as artifactual gradient in one direction result from the non-uniform illumination of screen or concentric pattern caused by limb darkening. We do not aim to achieve high accuracy in small-scale photometry, such as stellar photometry. Our basic approach to evaluate and calibrate the flat images is to observe the same sky area by different positions of the CCD, and to compare the measured brightness. Using the method described in Section A.2, we can easily evaluate the linear gradient errors of dome flat image. So we first evaluated this gradient and then assessed the other errors in Section A.3. Structure of Appendix A is as follows. In Section A.1 we present the observations. In Section A.2 we describe a method to evaluate the artifactual gradient. In section A.3 we show the results and assess the other error term. In section A.4 we present a summary of this chapter.

## A.1 Observations

The optical observations have been conducted on the 105cm Schmidt telescope with the 2KCCD camera at Kiso observatory in 2010 November 3-4. The telescope is equatorially mounted and its illustration is presented in Figure A.1. The 2KCCD camera has  $2048 \times 2048$  pixels with a pixel scale of  $1''.5 \text{ pixel}^{-1}$ , providing a field of view of  $50' \times 50'$ . The optical image data of target fields were taken in dark nights when the Moon was more than 40 degrees under the horizon. The average seeing was  $4''.0$ . The target fields are listed in Table A.1.

Each field was observed two different telescope attitudes with the same exposure times and the same number of exposures at the same field center. One attitude is called *north-up*, normally used for general observations. In the north-up mode, the y-axis of the CCD coordinates points to the north direction. The other mode is called *south-up* in which the y-axis of the CCD coordinates points to the south. The south-up mode is configured by flipping the telescope around the right ascension axis. The accuracy of the telescope pointing is a few arcminutes, i.e., each time we try to point the telescope to the same coordinate the center of the image may shift up to 200 pixels. On the Schmidt telescope at Kiso observatory, the observable area in the south-up mode is restricted to near the north

Table A.1 Optical observations

Field name	Field center (J2000)		Date (JST)	Observation time (JST)	Exposure (sec)	of exposures*	
	RA	Dec				B-band	R-band
Field 1	17h01m	+80D00	2010-11-03	18:03 - 18:51	120	2N, 2S	2N, 2S
Field 2	01h36m	+87D39	2010-11-03	18:54 - 20:07	120	3N, 3S	3N, 3S
Field 3	06h01m	+73D00	2010-11-03	21:48 - 23:12	120	4N, 4S	3N, 3S
Field 4 <sup>†</sup>	02h19m	+87D18	2010-11-04	18:30 - 19:47	300	2N, 2S	2N, 2S
Field 5 <sup>†</sup>	02h49m	+86D49	2010-11-04	19:51 - 21:09	300	2N, 2S	2N, 2S
Field 6 <sup>†</sup>	03h14m	+86D19	2010-11-04	21:13 - 23:34	300	2N, 2S	2N, 2S
Dome-Flat			2010-11-05	05:58 - 06:47	90	5N, 0S	5N, 0S

<sup>†</sup>Field 1 - 6 were observed in north-up and south-up telescope attitudes with the same number of exposures; “2N, 2S” means the field was observed twice each in north-up and south-up attitude. “5N, 0S” means the dome flat images were taken in the north-up mode only.

<sup>†</sup>Field 4 and 5, 5 and 6 are located adjacent to each other, as discussed in section 4.

celestial pole ( $\text{Dec} > 60^\circ$ ) and more than  $30^\circ$  from the culmination ( $|\text{hour angle}| > 2\text{h}$ ).

The observations are summarized in Table A.1. For each field we repeated following observation sequence: First we take one image at B- and R-band in the north-up mode, then flip the telescope and take one image at each band, then flip the telescope back to the north-up mode. The left panel of Figure A.2 shows a north-up image taken in Field 1. Most of the observed flux comes from the airglow. Thus, we use airglow emission as a stable light source. Actually, the absolute brightnesses of the airglow varies among the observations, however, the spatial brightness distribution was very stable while the same target field was observed. The typical signal-to-noise ratio at B- and R-band in a single 120 sec image is  $\sim 40$  per pixels and  $\sim 70$  per pixels, respectively.

The dome-flat screen is fixed to the dome and illuminated by a lamp manufactured by Kohoku Lighting Solutions Corporation. The screen is SORICSCREEN which was manufactured by Stellar Optics Research International Corporation. The illuminating light intensity is adjusted by neutral density filters to appropriate level for taking a dome flat image. The configuration of the illumination lamp, screen, and telescope is illustrated in Figure A.1.

The dome flat images were taken in the north-up mode only keeping the dome slit closed in order to avoid any leak of light into the dome. Five flat images per band were taken without moving the telescope or the dome, and coadded into a single dome flat image.

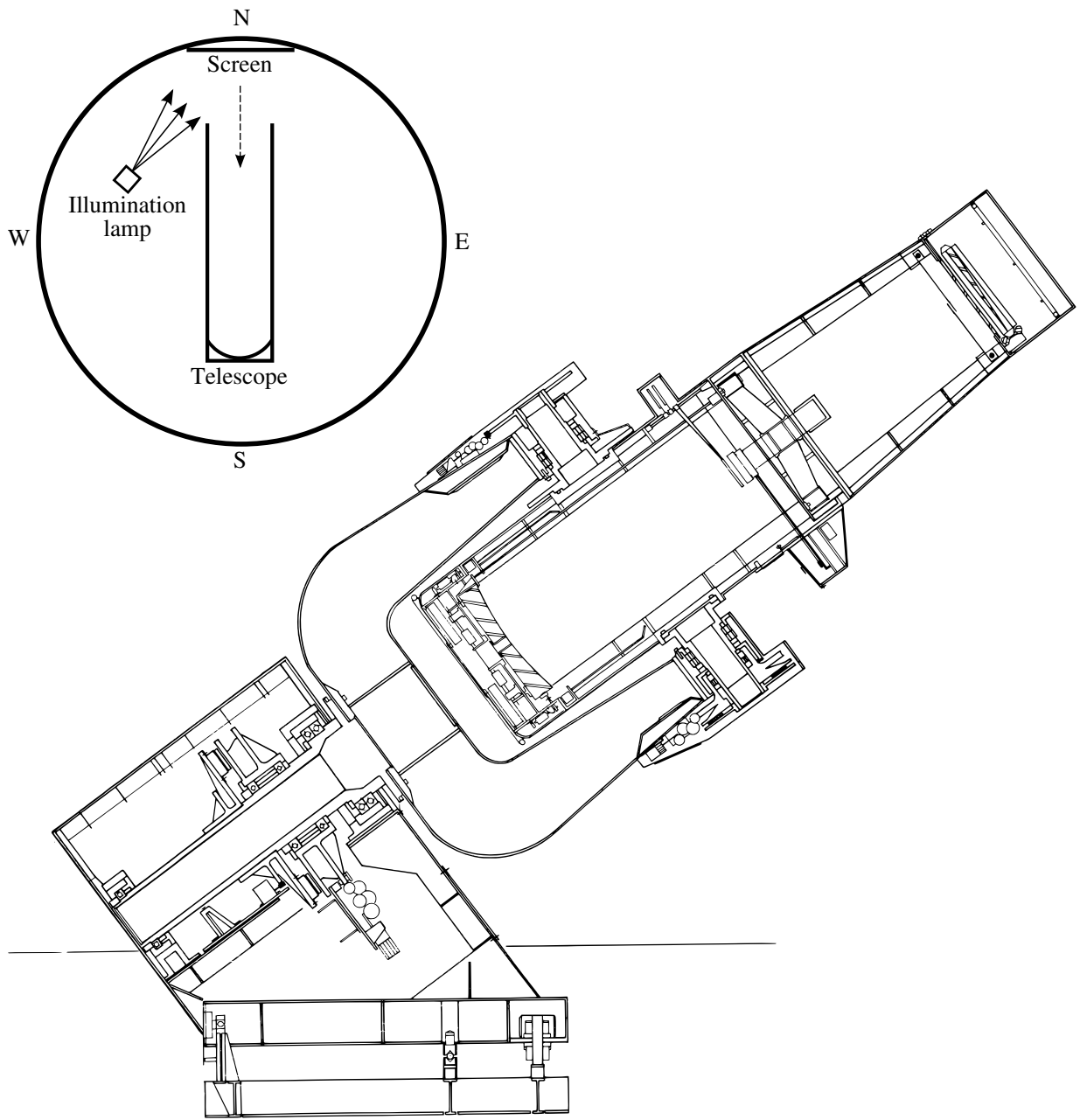


Figure A.1 Illustration of the 105cm Schmidt telescope at Kiso observatory. The upper left figure shows schematic configuration of the illumination lamp, screen, and telescope viewed from directly above.

## A.2 Method

The north-up image of target field  $N(x, y)$  can be expressed as:

$$N(x, y) = Sky(a, d)CCD(x, y)/flat(x, y), \quad (\text{A.1})$$

where  $(x, y)$  is the CCD coordinate with the zero-point at the center of the CCD array,  $(a, d)$  is the celestial coordinate correspond to the  $(x, y)$ . While the same target field was observed,  $(a, d)$  correspond one-to-one with  $(x, y)$ . In the north-up mode, the y-axis of the CCD coordinates points to the north direction and the x-axis points to the east direction.  $Sky(x, y)$  is the *real* brightness on the sky,  $CCD(x, y)$  is the sensitivity of the telescope-CCD system, and  $flat(x, y)$  is the dome flat image. In case of an ideal flat image, it is obviously

$$CCD(x, y)/flat(x, y) = C, \quad (\text{A.2})$$

where the  $C$  is a constant value. Because actual flat images are not ideal, we need to add a correction term  $\delta(x, y)$  as follows:

$$CCD(x, y)/flat(x, y) = C[1 + \delta(x, y)] \quad (\text{A.3})$$

Turning the hour angle by  $180^\circ$  switches the north-up image into the south-up, namely, changing  $CCD(x, y)/flat(x, y)$  to  $CCD(-x, -y)/flat(-x, -y)$ . Thus the south-up image  $S(x, y)$  of target field can be expressed as:

$$S(x, y) = Sky'(a, d)CCD(-x, -y)/flat(-x, -y) \quad (\text{A.4})$$

$$= Sky'(a, d)C[1 + \delta(-x, -y)]. \quad (\text{A.5})$$

The brightness of the sky is, in fact, not stable among the observation, thus the  $Sky(a, d)$  in equation (A.1) and  $Sky'(a, d)$  in equation (A.4) is not identical. However, if the spatial brightness distribution is stable, i.e.,  $Sky'(a, d) = Sky(a, d) \times Const.$ , we can write

$$S(x, y) = Sky(a, d)C[1 + \delta(-x, -y)], \quad (\text{A.6})$$

by scaling the observed images to the same level.

Here we separate  $\delta(x, y)$  for odd and even terms.

$$\delta(x, y) = \delta_O(x, y) + \delta_E(x, y), \quad (\text{A.7})$$

where  $\delta_O(x, y)$  and  $\delta_E(x, y)$  are odd and even terms, respectively, i.e.,  $\delta_O(x, y) = -\delta_O(-x, -y)$  and  $\delta_E(x, y) = \delta_E(-x, -y)$ .

Let a simple average of the north-up and south-up images be  $M(x, y)$ :

$$M(x, y) = [N(x, y) + S(x, y)]/2 \quad (\text{A.8})$$

$$= Sky(a, d)C[1 + \delta_E(x, y)] \quad (\text{A.9})$$

Now we divide the north-up image  $N(x, y)$  by the average image  $M(x, y)$  and we get

$$D_o(x, y) = \frac{1 + \delta_O(x, y) + \delta_E(x, y)}{1 + \delta_E(x, y)}. \quad (\text{A.10})$$

Assuming  $1 \gg \delta_O(x, y), \delta_E(x, y)$  results in

$$D_o(x, y) = 1 + \delta_O(x, y) \quad (\text{A.11})$$

$D_o$  is obtained simple arithmetic operations of observed images.  $\delta_O(x, y)$  can be expressed in a multinomial form, but in fact, terms of the third or higher degree are negligible as will be seen in Figure A.3. So we have,

$$\delta_O(x, y) = a_0x + a_1y. \quad (\text{A.12})$$

Then we determine  $(a_0, a_1)$  by fitting the right side of equation (A.11) to the obtained  $D_o$ .

### A.3 Results

Using the observed image, we obtained  $D_o$  images in the following way. First, the images of target fields were subtracted with the bias image and divided by the coadded dome flat image. The dark current of the CCD is negligible. Next, the images of the same target field were scaled to have the same value at  $(x, y) = (0, 0)$ . Then,  $M$  images were generated by north-up and south-up images are simply averaged. Finally, we obtained  $D_o$  by dividing the north-up image  $N$  by  $M$ . Note that, alignment for generating  $M$  and  $D_o$  images are performed by  $(a, d)$  coordinate, because  $(a, d)$  doesn't correspond one-to-one with  $(x, y)$  due to the limited accuracy of the telescope pointing. Therefore, the small-scale structure smaller than the pointing accuracy ( $\sim 5'$ ) can not be discussed in this analysis.

The two coefficients in equation (A.12) derived from the observed data are given in Table A.2 in units of CCD pixels number (i.e.,  $\text{pixels}^{-1}$ ). To derive the coefficients we fitted the right side of equation (A.11) to  $D_o$  of the each field separately. The coefficients and errors given in the Table A.2 are mean values and standard deviations of all the six fields. In the fitting process, we did not use 200 pixels from the edges of each field because these areas did not overlap among the images taken in the north-up and south-up mode due to the limited accuracy of the telescope pointing.

Figure A.2 shows north-up and  $D_o$  images in Field 1 centered (17h01m, 80D00). Figure A.3 shows the x- and y-profiles. We have coadded the  $D_o$  images in fields 1-6, and then averaged all the pixels in the y-direction (x-direction) to obtain the x-profile (y-profile). The right panel of Figure A.2 and indicates a linear gradient from the West to the East up to 1% per degree in the dome flat image.

The possible cause of linear gradient in the dome flat is asymmetric configuration of the lamp illuminating the screen. When we took the dome flat images, we illuminated the screen by a single lamp from the left side of the screen (see Figure A.1). The angular dependency of screen's scattering property would result in the liner gradient of the dome flat image.

To prevent this linear gradient error, we should divide science images (north-up images) with  $1 + \delta_O(x, y)$ , or simply average north-up and south-up images after applying the dome flat image.

After applying the correction for  $\delta_O(x, y)$ , the  $1 \sigma$  error is at worst at a rate of 0.10% and 0.12% per degree at B- and R- band, respectively. Thus, the  $\delta_O(x, y)$  correction reduces the flat-fielding accuracy by a factor of 10.

We also assess that the full scale of  $\delta_E(x, y)$  across the field of view is  $\sim \pm 0.2\%$  which is less than 1% obtained for  $\delta_O(x, y)$ . This assessment was performed in such a way that we compared the third quadrant of a  $\delta_O$ -corrected north-up image (Image A) with the first quadrant of an adjacent  $\delta_O$ -corrected north-up image (Image B). The positional relation of Image A and Image B is illustrated in the upper figure in Figure A.4, where Field 5 gives image B to Field 4 and image A to Field 6. We created images of  $F_A/F_B$ , where the  $F_A$  and  $F_B$  are the brightness on the sky measured in Image A and Image B, using the overlapped regions of Field 4 and Field 5, and Field 4 and Field 6. Before the dividing  $F_A$  and  $F_B$  are scaled to the same level using the mean value of the overlapped regions.

The lower panels of Figure A.4 are the the x- and y-profiles of  $\Delta(F_A/F_B) = F_A/F_B - 1$ . The x-profile (y-profile) were obtained by coadding the  $F_A/F_B$  images, and the averaging all the pixels in the y-direction (x-direction), same as Figure A.3. The flat-fielding error that results from the  $\delta_E(x, y)$  appears as the deviation from  $\Delta(F_A/F_B) = 0$ .

## A.4 Summary

We have described a method to measure and correct the artifactual gradient of the flat field image. By observing a field in two telescope attitudes with the same exposure times and the number of exposures at the same field center, we can evaluate the artifactual gradient. The dome flat image taken on the Schmidt telescope with the 2KCCD camera at

Table A.2 Correction term  $\delta_O(x, y)$

Coefficients in units of CCD pixels*		
	$a_0$ (pixels <sup>-1</sup> )	$a_1$ (pixels <sup>-1</sup> )
B-band	$(-6.70 \pm 0.16) \times 10^{-6}$	$(3.41 \pm 0.27) \times 10^{-6}$
R-band	$(-5.68 \pm 0.27) \times 10^{-6}$	$(1.58 \pm 0.40) \times 10^{-6}$

\*The coefficients in the equation of  $\delta_O(x, y) = a_0x + a_1y$  derived by the fitting.

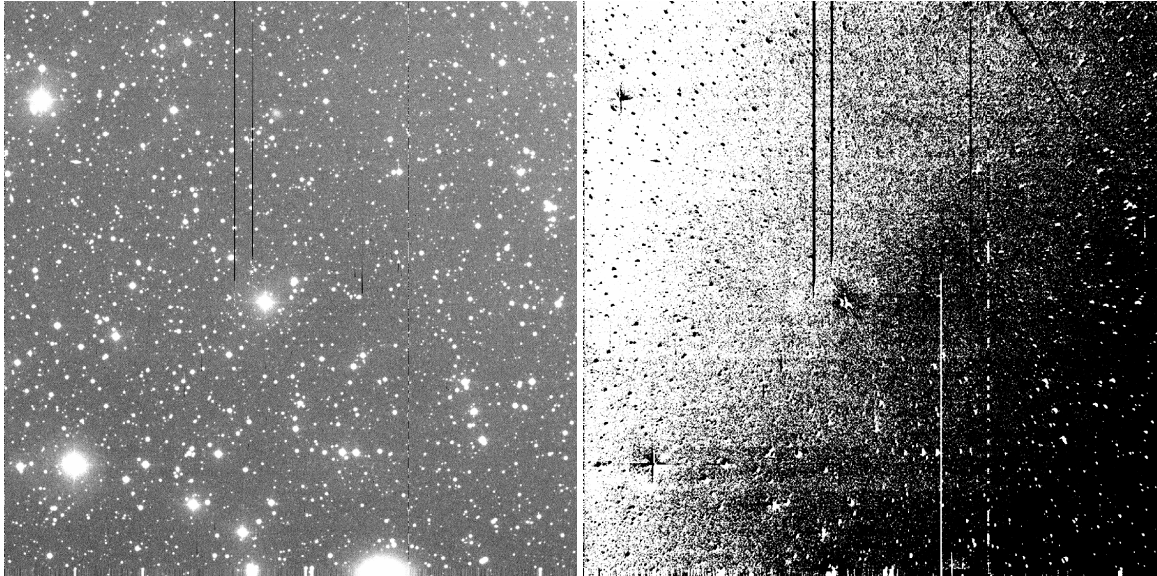


Figure A.2 The north-up (*left*) and  $D_o$  (*right*) images at R-band in Field 1. A gradient from the East to the West can be seen in  $D_o$  image. The vertical lines in both images are due to CCD defects.

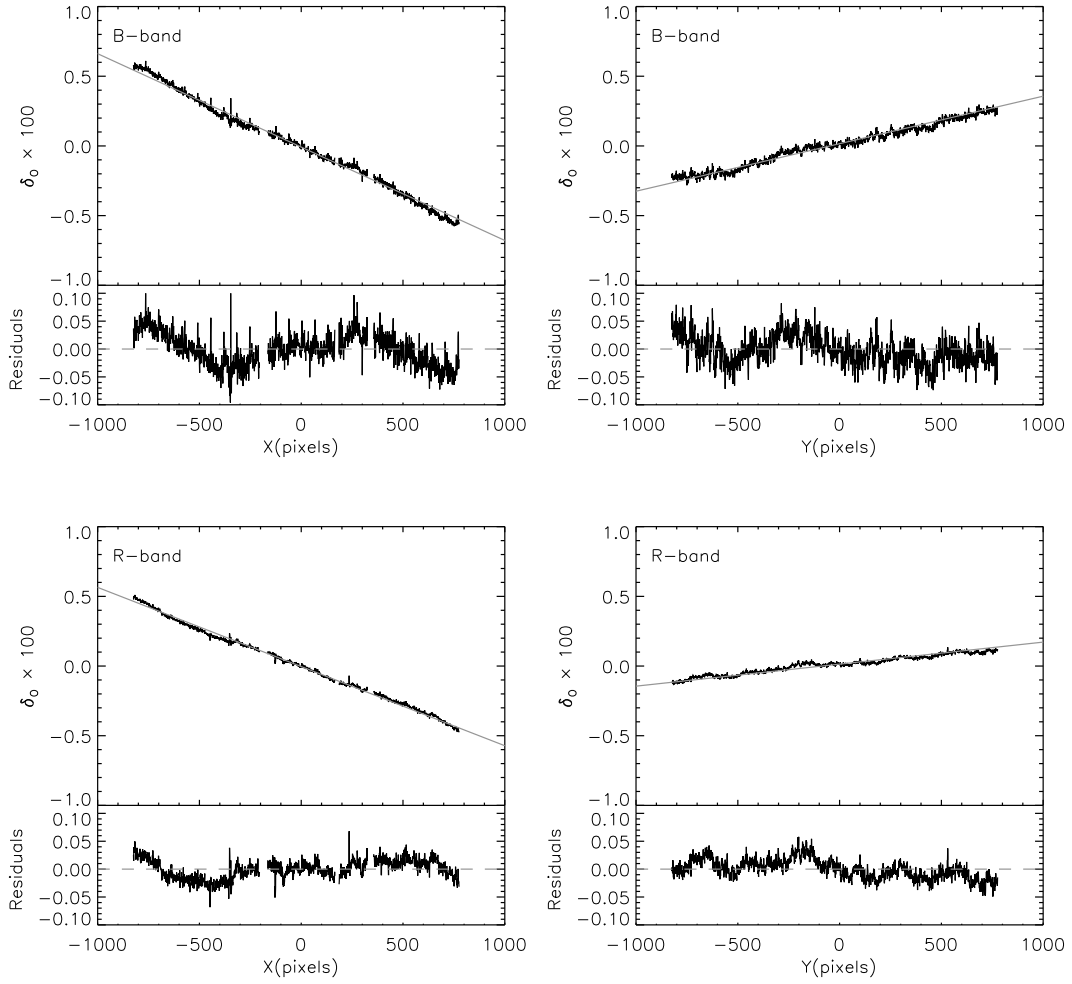


Figure A.3 The X- and Y- profiles of  $D_o$  images. The gray lines represent the same profiles of the  $\delta_O(x, y)$  obtained by the fitting (i.e, the plane expressed by the coefficients given in Table A.2). The residuals to the  $\delta_O(x, y)$  are shown in the bottom of each panel. The standard deviation of the residuals are 0.05%(B-band) and 0.04%(B-band) when binning the flame by  $1' \times 1'$ .

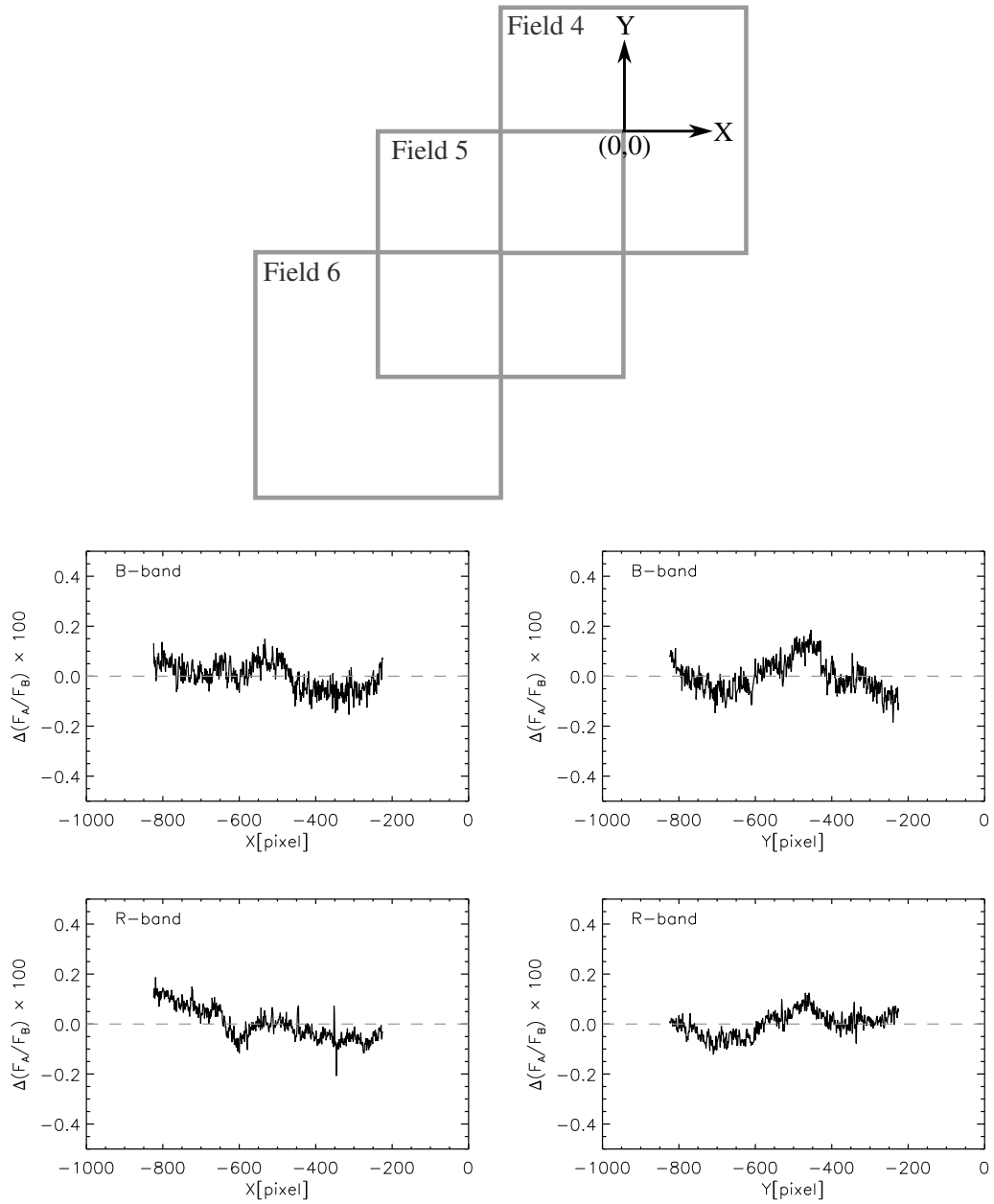


Figure A.4 The X- and Y- profiles of  $\Delta(F_A/F_B)$  images. The upper figure shows the positional relation of Image A and B; Image A is Field 4 (5) when compared with Field 5 (6), where the coordinate system has the origin at the center of Image A.

Kiso observatory have an artifactual gradient of  $\sim 1\%$  per degree, and after the correction the gradient could reduce the flat-fielding accuracy to  $\sim 0.2\%$ .

## Appendix B

# Radiative transfer in a dusty slab

Here we consider a simple model where a plane-parallel dust slab is illuminated at the backside by monochromatic starlight at optical wavelength  $\lambda$ . We measure optical depth  $\tau$  inward for the plane-parallel slab. Scattered light is produced along a sightline by the scattering of the starlight and the scattered light itself. Here, we assume completely forward-throwing scattering for simplicity. The contributions of an elements with optical depth from  $\tau$  to  $\tau + d\tau$  to the scattered light and the starlight are given by

$$dI_{\nu,sca}(\tau) = [I_{\nu,star}(\tau) + I_{\nu,sca}(\tau)]\omega d\tau - I_{\nu,sca}(\tau)d\tau \quad (\text{B.1})$$

$$dI_{\nu,star}(\tau) = -I_{\nu,star}(\tau)d\tau \quad (\text{B.2})$$

where  $I_{\nu,sca}(\tau)$  and  $I_{\nu,star}(\tau)$  are the specific intensity of the scattered light and the starlight, respectively,  $\omega$  is the albedo. Then the solution of  $I_{\nu,sca}(\tau)$  is given by

$$I_{\nu,sca}(\tau) = I_{\nu,star}(0) \exp[-(1 - \omega)\tau][1 - \exp(-\omega\tau)]. \quad (\text{B.3})$$

The far-infrared(IR) luminosity  $L(IR)$  comes from thermal emission from dust grains which absorb the starlight and the scattered light. The contribution of the elements to  $L(IR)$  is given by

$$dL_{\nu,IR}(\tau) \propto [I_{\nu,star}(\tau) + I_{\nu,sca}(\tau)](1 - \omega)d\tau. \quad (\text{B.4})$$

By integrating this equation, we have

$$L_{\nu,IR}(\tau) \propto I_{\nu,star}(0)\{1 - \exp[-(1 - \omega)\tau]\}. \quad (\text{B.5})$$

The conversion of the total IR luminosity to the  $100\mu\text{m}$  luminosity is  $L(100\mu\text{m}) = 0.52L(IR)$  which is applicable for models from 0.5 to 1.5 times the local ISRF intensity (Brandt & Draine 2012). Thus we have

$$b(\lambda) \propto \exp[-(1 - \omega)\tau][1 - \exp(-\omega\tau)]/\{1 - \exp[-(1 - \omega)\tau]\} \quad (\text{B.6})$$

where  $b(\lambda)$  is the intensity of the scattered light at wavelength  $\lambda$  relative to the intensity of  $100\mu\text{m}$  emission.

# Acknowledgements

I am most grateful to Kimiaki Kawara, my supervisor, for leading me with great patience. I thank Yoshiki Matsuoka, Hiroaki Smameshima, Naoko Asami, Shinki Oyabu, Takanori Shimizu, and Kei Sano for fruitful discussions.

I am grateful for the support provided by Kiso observatory. I wish to thank for T. Brandt for kindly providing their data in digital form as well as very useful comments and discussion. I also wish to thank for useful suggestion and support for B.A. Peterson, T. Tsujimoto.

Finally, I really appreciate the referees of this thesis, Takuya Yamashita, Yuzuru Yoshii, Naoteru Gouda, Ken Ebisawa, and Hideo Matsuhara for the elaborate, fruitful discussions and suggestions that significantly improved this thesis.

# Bibliography

- Aharonian, F., Akhperjanian, A. G., Bazer-Bachi, A. R., et al. 2006, *Nature*, 440, 1018
- Aihara, H., Allende Prieto, C., An, D., et al. 2011, *ApJS*, 193, 29
- Andersen, M. I., Freyhammer, L., & Storm, J. 1995, *Calibrating and Understanding HST and ESO Instruments*, 53, 87
- Bahcall, J. N., & Soneira, R. M. 1980, *ApJS*, 44, 73
- Beichman, C. A. 1987, *ARA&A*, 25, 521
- Bernstein, R. A. 2007, *ApJ*, 666, 663
- Bernstein, R. A., Freedman, W. L., & Madore, B. F. 2002, *ApJ*, 571, 56
- Bertin, E., & Arnouts, S. 1996, *A&AS*, 117, 393
- Brandt, T. D., & Draine, B. T. 2012, *ApJ*, 744, 129
- Broadfoot, A. L., & Kendall, K. R. 1968, *J. Geophys. Res.*, 73, 426
- Brown, T. M., Kimble, R. A., Ferguson, H. C., et al. 2000, *AJ*, 120, 1153
- Cambr esy, L., Reach, W. T., Beichman, C. A., & Jarrett, T. H. 2001, *ApJ*, 555, 563
- Capaccioli, M., & de Vaucouleurs, G. 1983, *ApJS*, 52, 465
- Caulet, A., Hook, R. N., & Fosbury, R. A. E. 1994, *A&AS*, 108, 271
- Cebula, R. P., & Feldman, P. D. 1982, *ApJ*, 263, 987
- Chamberlain, J. W. 1961, *International Geophysics Series*, New York: Academic Press, 1961

- Chromey, F. R., & Hasselbacher, D. A. 1996, *PASP*, 108, 944
- Darbon, S., Perrin, J.-M., & Sivan, J.-P. 1999, *A&A*, 348, 990
- Désert, F.-X., Abergel, A., Bernard, J.-P., et al. 1996, *American Institute of Physics Conference Series*, 348, 96
- Désert, F.-X., Boulanger, F., & Puget, J. L. 1990, *A&A*, 237, 215
- de Vries, C. P., & Le Poole, R. S. 1985, *A&A*, 145, L7
- Draine, B. T. 2003, *ARA&A*, 41, 241
- Dumont, R., & Sanchez, F. 1976, *A&A*, 51, 393
- Edelstein, J., Bowyer, S., & Lampton, M. 2000, *ApJ*, 539, 187
- Elvey, C. T., & Roach, F. E. 1937, *ApJ*, 85, 213
- Fardal, M. A., Katz, N., Weinberg, D. H., & Davé, R. 2007, *MNRAS*, 379, 985
- Fazio, G. G., Ashby, M. L. N., Barmby, P., et al. 2004, *ApJS*, 154, 39
- Feldman, P. D. 1977, *A&A*, 61, 635
- Frey, A., Hofmann, W., Lemke, D., & Thum, C. 1974, *A&A*, 36, 447
- Frey, A., Hofmann, W., & Lemke, D. 1977, *A&A*, 54, 853
- Furton, D. G., & Witt, A. N. 1990, *ApJ*, 364, L45
- Furton, D. G., & Witt, A. N. 1992, *ApJ*, 386, 587
- Gardner, J. P., Brown, T. M., & Ferguson, H. C. 2000, *ApJ*, 542, L79
- Gilmore, G., & Reid, N. 1983, *MNRAS*, 202, 1025
- Girardi, L., Groenewegen, M. A. T., Hatziminaoglou, E., & da Costa, L. 2005, *A&A*, 436, 895
- Gondhalekar, P. M. 1990, *The Galactic and Extragalactic Background Radiation*, 139, 49
- Gordon, K. D., Witt, A. N., & Friedmann, B. C. 1998, *ApJ*, 498, 522

- Gorjian, V., Wright, E. L., & Chary, R. R. 2000, *ApJ*, 536, 550
- Guhathakurta, P., & Tyson, J. A. 1989, *ApJ*, 346, 773
- Haikala, L. K., Mattila, K., Bowyer, S., et al. 1995, *ApJ*, 443, L33
- Hanner, M. S., Weinberg, J. L., DeShields, L. M., II, Green, B. A., & Toller, G. N. 1974, *J. Geophys. Res.*, 79, 3671
- Henyey, L. G., & Greenstein, J. L. 1941, *ApJ*, 93, 70
- Hofmann, W., Lemke, D., Thum, C., & Fahrbach, U. 1973, *Nature Physical Science*, 243, 140
- Hofmann, W., Lemke, D., & Thum, C. 1977, *Appl. Opt.*, 16, 3125
- Høg, E., Fabricius, C., Makarov, V. V., et al. 2000, *A&A*, 355, L27
- Itoh, N., Soyano, T., Tarusawa, K., et al. 2001, *Publications of the National Astronomical Observatory of Japan*, 6, 41
- Jester, S., Schneider, D. P., Richards, G. T., et al. 2005, *AJ*, 130, 873
- Jura, M. 1979, *ApJ*, 227, 798
- Kelsall, T., Weiland, J. L., Franz, B. A., et al. 1998, *ApJ*, 508, 44
- King, I. R. 1971, *PASP*, 83, 199
- Koch, A., Odenkirchen, M., Grebel, E. K., & Caldwell, J. A. R. 2004, *Astronomische Nachrichten*, 325, 299
- Lagache, G., & Puget, J. L. 2000, *A&A*, 355, 17
- Lasker, B. M., Lattanzi, M. G., McLean, B. J., et al. 2008, *AJ*, 136, 735
- Laureijs, R. J., Mattila, K., & Schnur, G. 1987, *A&A*, 184, 269
- Lehtinen, K., Juvela, M., Mattila, K., Lemke, D., & Russeil, D. 2007, *A&A*, 466, 969
- Leinert, C., Bowyer, S., Haikala, L. K., et al. 1998, *A&AS*, 127, 1
- Leinert, C., & Grun, E. 1990, *Physics of the Inner Heliosphere I*, 207
- Leinert, C., & Richter, I. 1981, *A&AS*, 46, 115

- Levasseur-Regourd, A. C. 1996, IAU Colloq. 150: Physics, Chemistry, and Dynamics of Interplanetary Dust, 104, 301
- Levasseur-Regourd, A. C., & Dumont, R. 1980, *A&A*, 84, 277
- Lillie, C. F. 1972, Scientific results from the orbiting astronomical observatory (OAO-2), 310, 95
- Low, F. J., Young, E., Beintema, D. A., et al. 1984, *ApJ*, 278, L19
- Madau, P., & Pozzetti, L. 2000, *MNRAS*, 312, L9
- Magnani, L., Blitz, L., & Mundy, L. 1985, *ApJ*, 295, 402
- Magnani, L., & de Vries, C. P. 1986, *A&A*, 168, 271
- Magnani, L., Hartmann, D., & Speck, B. G. 1996, *ApJS*, 106, 447
- Manfroid, J. 1995, *A&AS*, 113, 587
- Mathis, J. S., Mezger, P. G., & Panagia, N. 1983, *A&A*, 128, 212
- Matsumoto, T., Matsuura, S., Murakami, H., et al. 2005, *ApJ*, 626, 31
- Matsuoka, Y., Ienaka, N., Kawara, K., & Oyabu, S. 2011, *ApJ*, 736, 119
- Matsuura, S., Matsumoto, T., Matsuhara, H., & Noda, M. 1995, *ICARUS*, 115, 199
- Mattila, K. 1979, *A&A*, 78, 253
- Mattila, K. 1980, *A&AS*, 39, 53
- Mattila, K. 1990, *The Galactic and Extragalactic Background Radiation*, 139, 257
- Mattila, K., Schnur, G, see Mattila, 1990
- Mattila, K. 2003, *ApJ*, 591, 119
- Maucherat-Joubert, M., Deharveng, J. M., & Cruvellier, P. 1979, *A&A*, 74, 218
- Moffat, A. F. J. 1969, *A&A*, 3, 455
- Morgan, D. H., Nandy, K., & Thompson, G. I. 1976, *MNRAS*, 177, 531
- Murakami, H., Baba, H., Barthel, P., et al. 2007, *PASJ*, 59, 369

- Murdock, T. L., & Price, S. D. 1985, *AJ*, 90, 375
- Nishimura, T. 1973, *PASJ*, 25, 375
- Orear, J. 1982, *American Journal of Physics*, 50, 912
- Paley, E. S., Low, F. J., McGraw, J. T., Cutri, R. M., & Rix, H.-W. 1991, *ApJ*, 376, 335
- Perrin, J.-M., & Sivan, J.-P. 1992, *A&A*, 255, 271
- Pitz, E., Leinert, C., Schulz, A., & Link, H. 1979, *A&A*, 74, 15
- Roach, F. E., & Gordon, J. L. 1973, Dordrecht, Boston, Reidel [1973],
- Schlegel, D. J., Finkbeiner, D. P., & Davis, M. 1998, *ApJ*, 500, 525
- Sparrow, J. C., & Ney, E. P. 1972, *ApJ*, 174, 705
- Sparrow, J. G., & Ney, E. P. 1972, *ApJ*, 174, 717
- Stark, R. 1995, *A&A*, 301, 873
- Szomoru, A., & Guhathakurta, P. 1998, *ApJ*, 494, L93
- Tennyson, P. D., Henry, R. C., Feldman, P. D., & Hartig, G. F. 1988, *ApJ*, 330, 435
- Totani, T., Yoshii, Y., Iwamuro, F., Maihara, T., & Motohara, K. 2001, *ApJ*, 550, L137
- Uson, J. M., Boughn, S. P., & Kuhn, J. R. 1991, *ApJ*, 369, 46
- van de Hulst, H. C., & de Jong, T. 1969, *Physica*, 41, 151
- Van de Noord, E. L. 1970, *ApJ*, 161, 309
- Vrtilek, J. M., & Hauser, M. G. 1995, *ApJ*, 455, 677
- Weingartner, J. C., & Draine, B. T. 2001, *ApJ*, 548, 296
- Witt, A. N., & Boroson, T. A. 1990, *ApJ*, 355, 182
- Witt, A. N., Friedmann, B. C., & Sasseen, T. P. 1997, *ApJ*, 481, 809
- Witt, A. N., Gordon, K. D., Vihj, U. P., et al. 2006, *ApJ*, 636, 303

- Witt, A. N., Mandel, S., Sell, P. H., Dixon, T., & Vihj, U. P. 2008, *ApJ*, 679, 497
- Witt, A. N., & Petersohn, J. K. 1994, *The First Symposium on the Infrared Cirrus and Diffuse Interstellar Clouds*, 58, 91
- Witt, A. N., & Schild, R. E. 1985, *ApJ*, 294, 225
- Witt, A. N., & Schild, R. E. 1988, *ApJ*, 325, 837
- Witt, A. N., Schild, R. E., & Kraiman, J. B. 1984, *ApJ*, 281, 708
- Wright, E. L. 2001, *ApJ*, 553, 538
- Wright, E. L. 2004, *New Astronomy Reviews*, 48, 465
- Zagury, F. 2006, *MNRAS*, 370, 1763
- Zagury, F., Boulanger, F., & Banchet, V. 1999, *A&A*, 352, 645
- Zubko, V., Dwek, E., & Arendt, R. G. 2004, *ApJS*, 152, 211